Available online at www.sciencedirect.com

ScienceDirect

Underground Space 27 (2026) 424–444

www.keaipublishing.com/undsp

Research Paper

Experimental study on mechanism of soil arching effect induced by vertical unloading in deep underground construction

Xing-Tao Lin [a,b,c,d], Deng Wang [a], Dong Su [a,b,c,d,*], Hui Zeng [a],
Ruixiao Zhang [a,b,c,d], Xiangsheng Chen [a,b,c,d]

[a] *College of Civil and Transportation Engineering, Shenzhen University, Shenzhen 518061, China*
[b] *Key Laboratory for Resilient Infrastructures of Coastal Cities (MOE), Shenzhen University, Shenzhen 518060, China*
[c] *State Key Laboratory of Intelligent Geotechnics and Tunnelling, Shenzhen 518060, China*
[d] *Underground Polis Academy, Shenzhen University, Shenzhen 518060, China*

Received 9 June 2025; received in revised form 30 November 2025; accepted 16 December 2025
Available online 9 February 2026

Abstract

As shallow underground resources are depleted, urban development is extending to greater depths, necessitating a clear understanding of soil arching at various burial depth conditions. Laboratory trapdoor tests equipped with embedded soil–pressure cells and digital image correlation captured the ground–reaction curve and soil deformation. The results reveal pronounced discrepancies between shallow and deep burial. In shallow conditions, soil arching undergoes a "failure-reconstruction" process: soil pressure plunges, then rebounds to stability. In deep strata, the arching forms rapidly and attains stability almost immediately after the minimum pressure is reached. Shallow tests generate several horizontal displacement bands rising to 4.8*B* (*B*, trapdoor width); deep tests yield one stable band, with its influence height reduced to about 3.0*B*. Vertical displacement above the trapdoor evolves through "triangular-tower-parabolic" stages to 4.3*B* in shallow tests, but follows a persistent parabolic profile limited to 2.7*B* in deep tests. Additionally, shear bands under deep conditions form at smaller angles and are more vertically oriented. These findings expose the fundamental differences in deformation mechanisms between shallow and deep burial and provide quantitative criteria for depth zoning in urban underground space development.

Keywords: Soil arching; Trapdoor test; Digital image correlation; Deep burial

---

1 Introduction

With the acceleration of urbanization and the increasing demand for underground space, shallow subsurface resources have become depleted, making deep underground development an inevitable trend for megacities. Large-scale infrastructures such as high-rise building foundations and urban tunnels often extend tens to hundreds of meters below the ground surface (Costa & Zornberg, 2020; Zhang et al., 2016). During deep-space development, construction-induced differential settlement significantly affects the formation and evolution of soil arching and leads to stress strain redistribution in the surrounding soil (Consoli et al., 2018; Handy, 1985; Zhang et al., 2016). Soil arching, a key mechanical phenomenon in geotechnical engineering, arises from stress redistribution caused by localized differential displacement and plays a crucial role in load transfer in tunnels, pile foundations, and deep underground construction (Handy, 1985; Terzaghi, 1943; Wang & Chen, 2019).

---

[*] Corresponding author at: College of Civil and Transportation Engineering, Shenzhen University, Shenzhen 518061, China.
E-mail address: sudong@szu.edu.cn (D. Su).

Peer review under the responsibility of Tongji University

https://doi.org/10.1016/j.undsp.2025.12.003

Research on soil arching originated with Janssen's mechanical model for granular materials and was subsequently validated and expanded by Terzaghi through trapdoor tests, forming the classical theoretical framework. Building on this foundation, da Silva Burke and Elshafie (2021) derived an analytical expression for the lateral coefficient K using a centrifuge trapdoor model, refining parameter selection in classical theory and providing a more general basis for later studies. Extensive engineering investigations have since examined soil arching in various applications, including pile foundations (Han & Gabr, 2002; Hu et al., 2024; Rui et al., 2019), shield tunnels (Bi et al., 2020; Chevalier et al., 2012; Costa & Zornberg, 2020; Wu et al., 2022), buried pipelines (Lim & Ou, 2017), and slopes (Fang et al., 2024; Kourkoulis et al., 2011). For instance, Cao et al. (2024) conducted 3D model tests to quantify soil arching evolution, stress concentration ratios, and equal-settlement-plane height in pile-supported embankments. Song et al. (2025) demonstrated, through deep-buried shield tunneling tests and simulations, that excavation induces pronounced soil arching, characterized by stress concentration, unloading zones, and depth-dependent arch morphology. Zhang et al. (2023), combining trapdoor tests with digital image correlation (DIC), demonstrated that existing tunnels weaken the final arching effect, particularly with greater overburden depth. Song et al. (2023) numerically verified soil arching under deep saturated shield conditions and proposed criteria for distinguishing arching and loosening zones. Chen et al. (2025) conducted deep shield tunnel model tests and found that ground reaction curves exhibited two-stage reductions during tunnel convergence, and shear band inclination decreased under higher stress levels due to enhanced soil dilatancy suppression. In summary, existing research has primarily focused on shallow burial conditions. Although several studies have explored soil arching at greater depths, the distinctive mechanical differences between shallow and deep conditions remain insufficiently understood. Deep soil layers typically exhibit higher initial stresses and stronger inter-particle cementation, resulting in markedly different arching characteristics and progressive failure modes. Therefore, clarifying soil arching formation and degradation mechanisms in deep soils is essential for the safe and sustainable utilization of deep underground urban spaces.

Consequently, this study aims to elucidate the evolution of soil arching under shallow and deep conditions using a custom-designed apparatus capable of simulating ground failure under extreme loading conditions. The results reveal the influence of burial depth on soil arching formation and degradation, identify distinct load-transfer mechanisms and deformation patterns corresponding to varying depths, and provide fundamental insights and practical guidance for deep tunnel stability assessment and underground infrastructure design.

2 Experimental tests

2.1 Test equipment

The independently developed experimental apparatus for simulating ground failure under extreme conditions is illustrated in Fig. 1(a). It comprises six main components:

1. Model chamber (Fig. 1(b)) measures 1200 mm (length) × 400 mm (width) × 1060 mm (height). To enable optical soil deformation measurement, one side features a high-strength acrylic observation window (840 mm × 660 mm × 200 mm) installed flush with the steel wall to eliminate local discontinuities and ensure uniform lateral confinement.
2. Soil-pressure loading device (Fig. 1(c)), comprising a loading plate and reaction frame, can apply ground stresses simulating up to 120 m burial depth, with a maximum force of 900 kN (~92 t). Synchronous five-axis connections between the plate and frame ensure uniform load transmission to the soil sample.
3. A trapdoor system (Fig. 1(d)), located centrally at the chamber bottom, the trapdoor (400 mm × 100 mm; length matches chamber width to maintain plane strain) is spaced $5.5B$ from sidewalls to minimize boundary effects. The system comprises three independently controlled trapdoors, permitting maximum displacements of 200 mm (central) and 100 mm (side). All trapdoors are servo-driven with speed adjustment, and integrated displacement sensors enable real-time, precise monitoring and control. In this study, only the central trapdoor was used.
4. Hydraulic station (Fig. 1(e)) provides hydraulic power to both the soil-pressure loading and trapdoor servo systems.
5. Comprehensive control system (Fig. 1(f)) enables unified, intelligent management of the soil-pressure loading, water-pressure loading, and trapdoor displacement subsystems.
6. Data acquisition (Fig. 1(g)) monitors and records soil pressure at 10 Hz throughout testing.

2.2 Measurement system

In this study, soil pressure sensors were used to monitor soil pressure variations, while DIC was employed to track soil displacement. This experimental approach parallels that of da Silva Burke and Elshafie (2021), who applied particle image velocimetry (PIV) in a centrifuge trapdoor model to synchronously capture deformation images and ground reaction curves. DIC, a non-contact optical measurement technique, was implemented using VIC 2D to compute incremental displacement fields. Soil deformation images were captured through the transparent acrylic

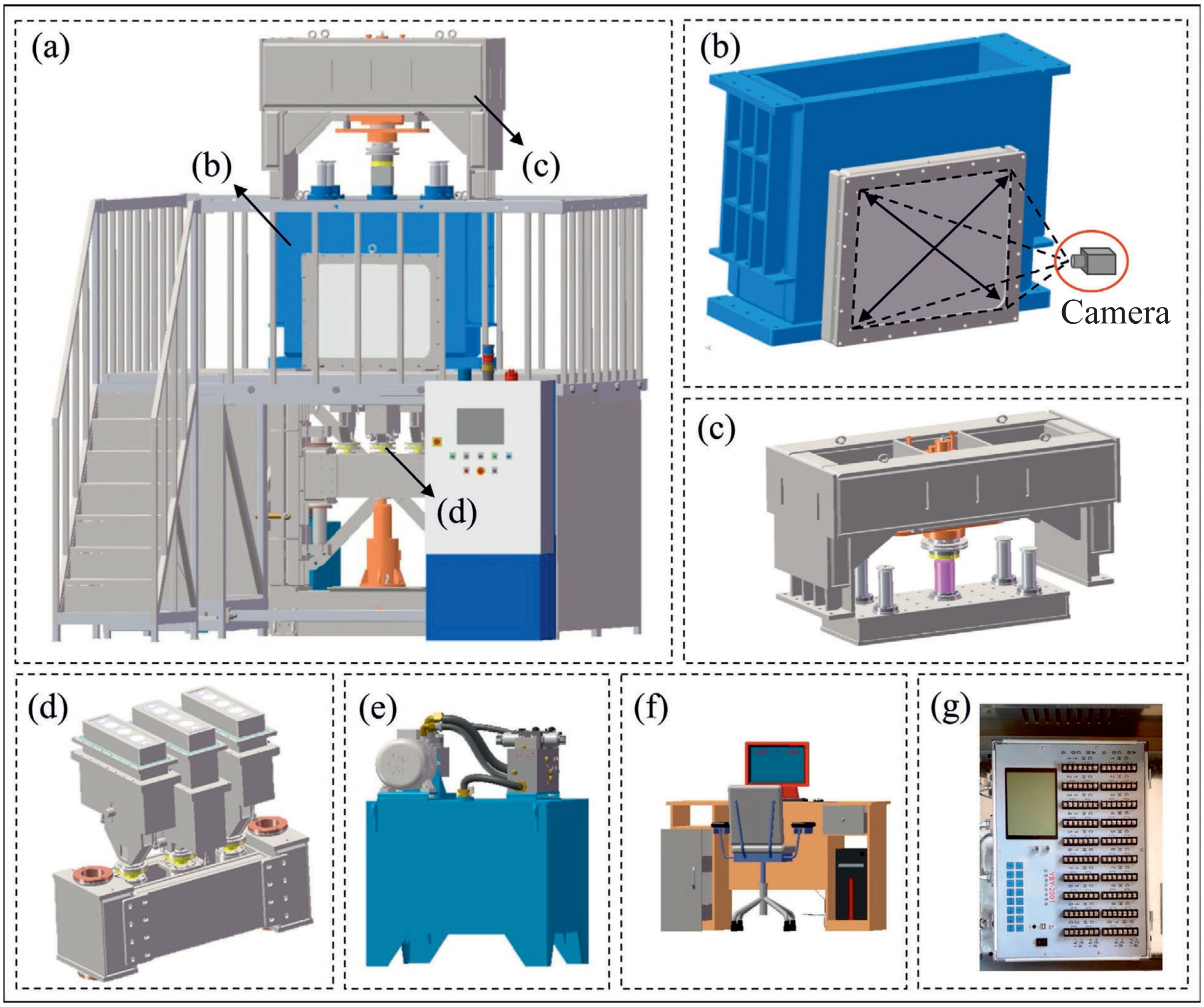

Fig. 1. Experimental apparatus for simulating ground failure under extreme conditions. (a) Experimental apparatus, (b) model chamber, (c) soil-pressure loading device, (d) trapdoor system, (e) hydraulic station, (f) comprehensive control system, and (g) data acquisition.

observation window using a Sony ZV E10 camera at 5 second intervals, enabling continuous monitoring of soil movement.

For DIC acquisition, a natural high-contrast speckle pattern was achieved by layering colored sand. Correlation analysis parameters were set as follows: subset size 111 pixels (optimized for 0.01-pixel matching accuracy at the measured noise level), step size 27 pixels, and outlier threshold, confidence interval, and correlation quality threshold all at 0.5 pixels. A filter size of 15 was applied during strain computation to suppress random noise. The image resolution was 6000 pixels × 4000 pixels, with an analysis area (AOI) of 750 mm × 500 mm. These configurations ensured high-precision, efficient tracking of displacement and strain fields.

As depicted in Fig. 2, 33 soil pressure sensors were embedded at the chamber base to monitor soil stress distribution in real time. To minimize monitoring interference from unintended arching effects near the sensors, they were installed flush with the chamber base—either directly embedded in the trapdoors or arranged drawer-style in the chamber floor. Each trapdoor was equipped with three sensors positioned at the center (Sensor 5), left edge (Sensor 6), and right edge (Sensor 4), with 30 mm center-to-center spacing. Side trapdoors used the same layout as the central trapdoor. Sensors 22–26 were placed between the left and central trapdoors, with sensor 26 located 120 mm from the central trapdoor edge. Sensors 27–33 were located outside the left-side trapdoor. The chamber's right side mirrored this sensor configuration, yielding a fully symmetric sensor layout. Key technical specifications of the sensors are provided in Table 1.

Prior to testing, all earth pressure sensors were calibrated via the hydrostatic pressure method. As shown in Fig. 3, all sensors demonstrated excellent linearity and stable sensitivity across the working range, with measurement errors within ±0.5% F.S. Due to the large number of sensors, only representative calibration results are presented in the figure.

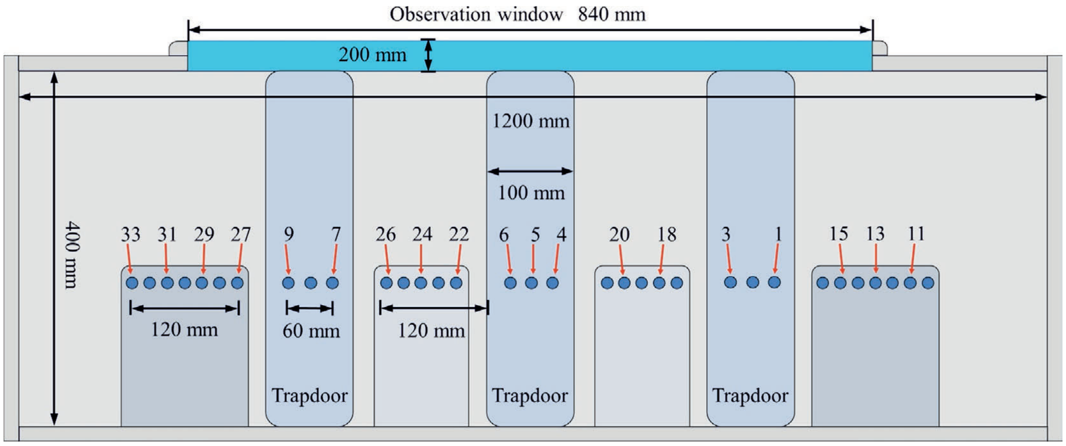

Fig. 2. Schematic of sensor layout and DIC image acquisition.

Table 1
Main technical specifications of the sensor.

Key technical parameters	Parameter description
Measuring range (MPa)	0–3 MPa
Accuracy	0.5%F.S.
Dimensions (mm)	Φ11
Operating temperature range (°C)	–35 to +80
Compatible strain amplifier sensitivity coefficient (K)	2.00
Overload capacity (%)	Capable of continued operation at 120% of the rated range

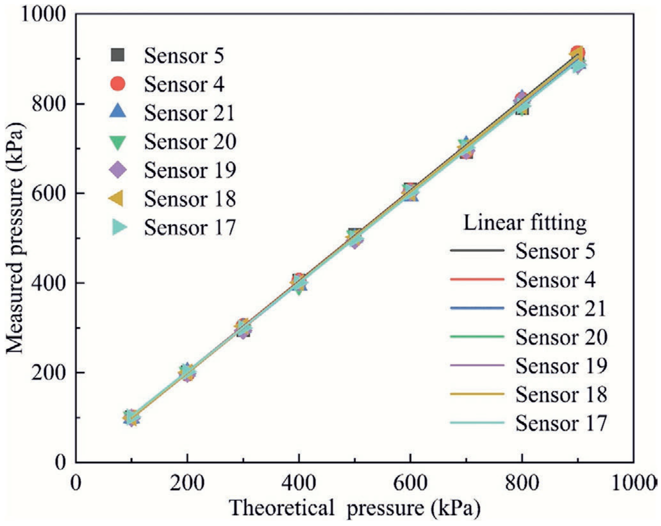

Fig. 3. Calibration results of soil pressure sensors.

2.3 Granular material

The sand used in the tests was marine sand sourced from Beihai, Guangxi Province, China, with an average particle size (d_{50}) of 0.32 mm. Triaxial compression tests were conducted, yielding an effective internal friction angle of 34°. Given that the maximum particle size of the sand did not exceed 5 mm, the minimum and maximum dry densities of the sand were measured using the funnel method and vibrating hammer compaction method, yielding values of 1.29 and 1.72 g/cm^3, respectively. Particle size distribution analyses were performed through sieve tests, and the gradation curve is presented in Fig. 4.

2.4 Testing procedure

As summarized in Table 2, five sets of model tests were conducted in the model chamber, all controlled at the same relative density ($D_r = 80\%$), corresponding to a dry density (ρ_d) of 1.634 g/cm^3. By uniformly applying vertical loading on the sand specimen through the loading plate, various burial depths were simulated. The simulated burial depth (H) and corresponding loading pressure (P) were calculated using the following relationship:

$$H = \frac{P}{\rho_d g S}, \tag{1}$$

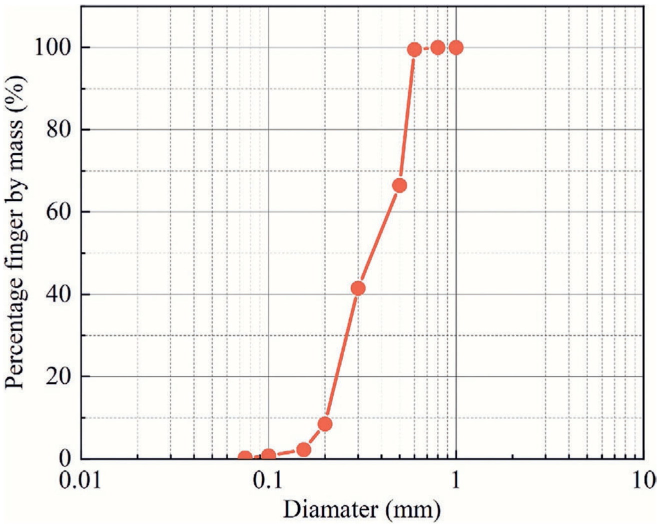

Fig. 4. Particle size distribution curve of the test sand.

where H is the simulated burial depth, ρ_d is the dry density of the sand fill, g is the gravitational acceleration, and S is the bottom area of the model chamber. For example, at a simulated burial depth of 10 m, the required loading pressure P was calculated as $P = 10 \times 1.634 \times 9.8 \times 0.48 \approx 77$ kN. The loading pressures corresponding to other burial depths are detailed in Table 2, where test numbers B10, B30, etc., denote simulated burial depths of 10 m, 30 m, and so forth.

Figure 5 presents the experimental procedure:

(1) Step 1: Test preparation. All apparatus systems were checked, sensors installed and verified, and the chamber walls were coated with industrial lubricant (Fig. 5 (a)) to reduce sand-wall friction and minimize boundary effects. Each sensor was covered with ultrafine sand (Fig. 5(b)) to mitigate local arching effects and enhance measurement accuracy.

(2) Step 2: Soil filling. The soil sample was prepared in eight 100 mm layers, each filled with 78.4 kg of sand, distributed evenly, and compacted with a rubber mallet to achieve a target relative density of 80% and minimize vibration. Colored sand layers were placed before the first five layers (Fig. 5(c)) to facilitate DIC monitoring. After all layers were placed (Fig. 5 (d)), the sample was left to stand for six hours for stabilization.

(3) Step 3: Loading system installation. The loading plate was positioned (Fig. 5(e)) and then bolted to the chamber. The reaction frame was attached (Fig. 5 (f)), and the control system applied and maintained the designated pressure for six hours.

(4) Step 4: Testing started. The DIC camera system was set up, and the trapdoor was lowered at the specified rate (Table 2) via the control system (Fig. 5(g)), with upper loading pressure sustained. Images were captured for every 0.1 mm of trapdoor displacement; soil pressure sensors recorded at 10 Hz until a 150 mm displacement was reached. The final soil state is shown in Fig. 5(h).

Table 2
Test program.

Test label	Backfill height (mm)	Pressure (kN)	Burial depth (m)	Speed (mm/min)
B10	800	77	10	1.2
B30	800	230	30	1.2
B50	800	384	50	1.2
B70	800	538	70	1.2
B90	800	692	90	1.2

3 Test results

To assess the uniformity of the initial overburden stress field, vertical soil pressure readings from all sensors were extracted prior to loading under each test condition. As shown in Fig. 6, the results reveal an approximately uniform initial vertical stress distribution across the sensor array, validating the use of initial readings for normalization. This uniformity further confirms that the overburden stress field produced by the rigid loading plate closely matches the theoretical self-weight distribution.

3.1 Variation of soil pressure on the trapdoor

The ground reaction curve (GRC) is a key tool for analyzing the relationship between trapdoor displacement and soil loading, revealing how soil arching evolution relates to

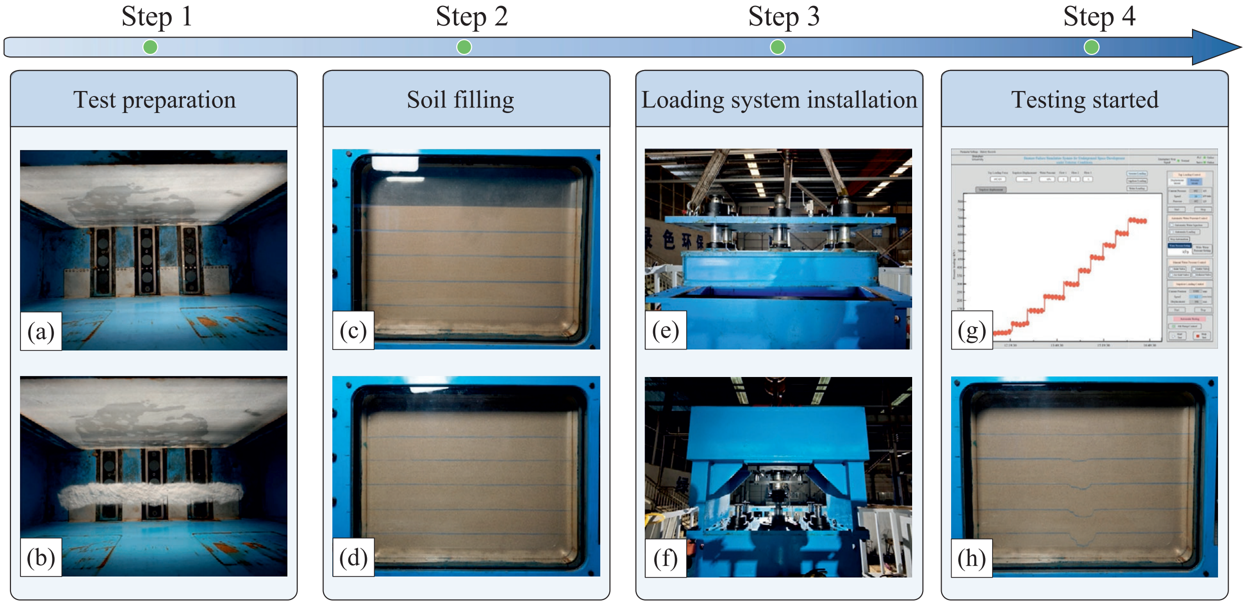

Fig. 5. Experimental procedure. (a) Pre-test preparation, (b) placement of ultrafine sand, (c) soil filling, (d) completion of backfill, (e) installation of the loading plate, (f) installation of the reaction frame, (g) control system, and (h) trapdoor fully lowered.

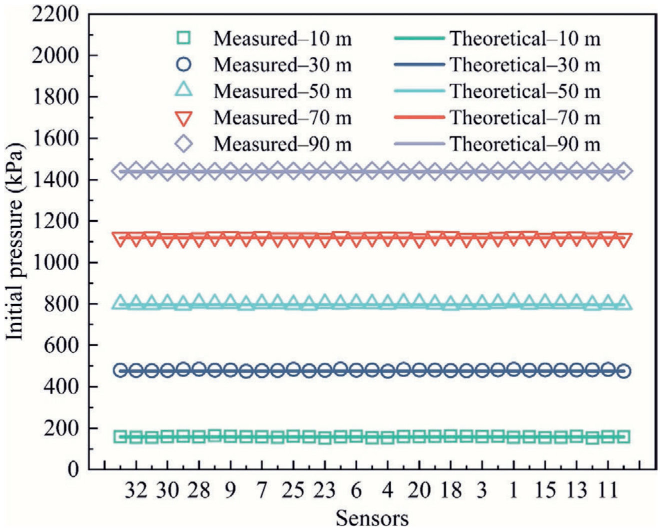

Fig. 6. Comparison between measured and theoretical vertical soil pressure distributions before loading.

changes in soil pressure (Lin et al., 2022). Figure 7 presents the relationship between soil pressure above the trapdoor and trapdoor displacement for different simulated burial depths (10, 30, 50, 70, and 90 m). Both soil pressure and displacement (δ) are normalized by initial overburden pressure and trapdoor width (B), respectively. As burial depths were simulated using a vertical loading system, initial overburden pressures for normalization were taken directly from sensor readings, following Zhang et al. (2023). The normalized soil pressure, known as the soil arching ratio, characterizes the variation of soil pressure during the process.

With increasing trapdoor displacement, the soil arching ratio initially exhibited a sharp decline, after which two distinct evolutionary trends were observed:

(1) Under burial depths of 10 m and 30 m, the arching ratio enters a rebound phase after reaching its minimum. However, distinct differences emerge thereafter. For the 10 m condition, the arching ratio

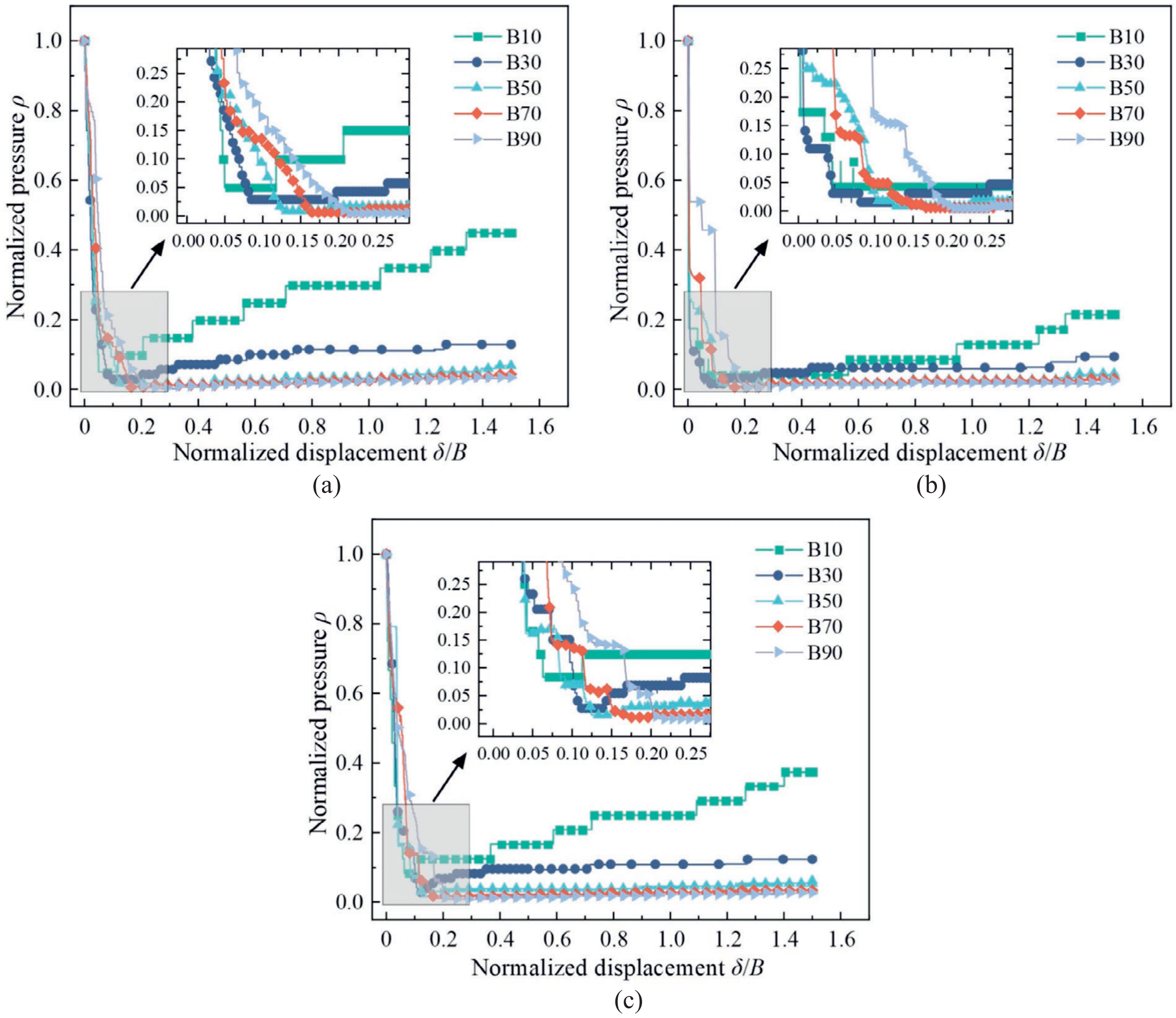

(a)

(b)

(c)

Fig. 7. Variation of normalized pressure with normalized displacement on the trapdoor. (a) Sensor 4, (b) Sensor 5, and (c) Sensor 6.

exhibits a discrete “stepwise increase” beyond approximately 80% normalized displacement. This behavior reflects the susceptibility of frictional granular media to intermittent force chain reorganization and localized slippage under low confining pressure, leading to staged stress redistribution and repeated reconstruction of the soil arch. Meanwhile, the central sensor (Sensor 5) on the trapdoor records a notably higher and more stable normalized pressure during the stepwise rebound phase compared to the edge sensors (Sensors 4 and 6), suggesting that the arch edges are more vulnerable to stress concentration during reconstruction, resulting in differentiated responses between the center and edges. In contrast, the rebound process at 30 m is smoother and stabilizes at around 80% displacement. This is attributed to the relatively low initial stress at 30 m, which still falls within the shallow burial regime. As the trapdoor descends, the soil more readily enters a plastic state, leading to cycles of arch failure and reconstruction. Nevertheless, signs of transition toward deep-burial behavior begin to emerge.

(2) For greater burial depths (50, 70, 90 m), the soil arching ratio stabilized immediately after reaching its minimum without any noticeable rebound, achieving stability at approximately 30% normalized displacement. This indicates that higher initial stresses at greater depths restrict the extent of the plastic zones; once formed, the soil arching structure remains stable, minimizing the effect of further trapdoor displacement.

3.2 Variation of soil pressure beside the trapdoor

In addition to the vertical soil pressure directly above the trapdoor, lateral soil pressure variations of the trapdoor offer insight into the propagation characteristics of the soil arching effect. Figure 8 illustrates the normalized

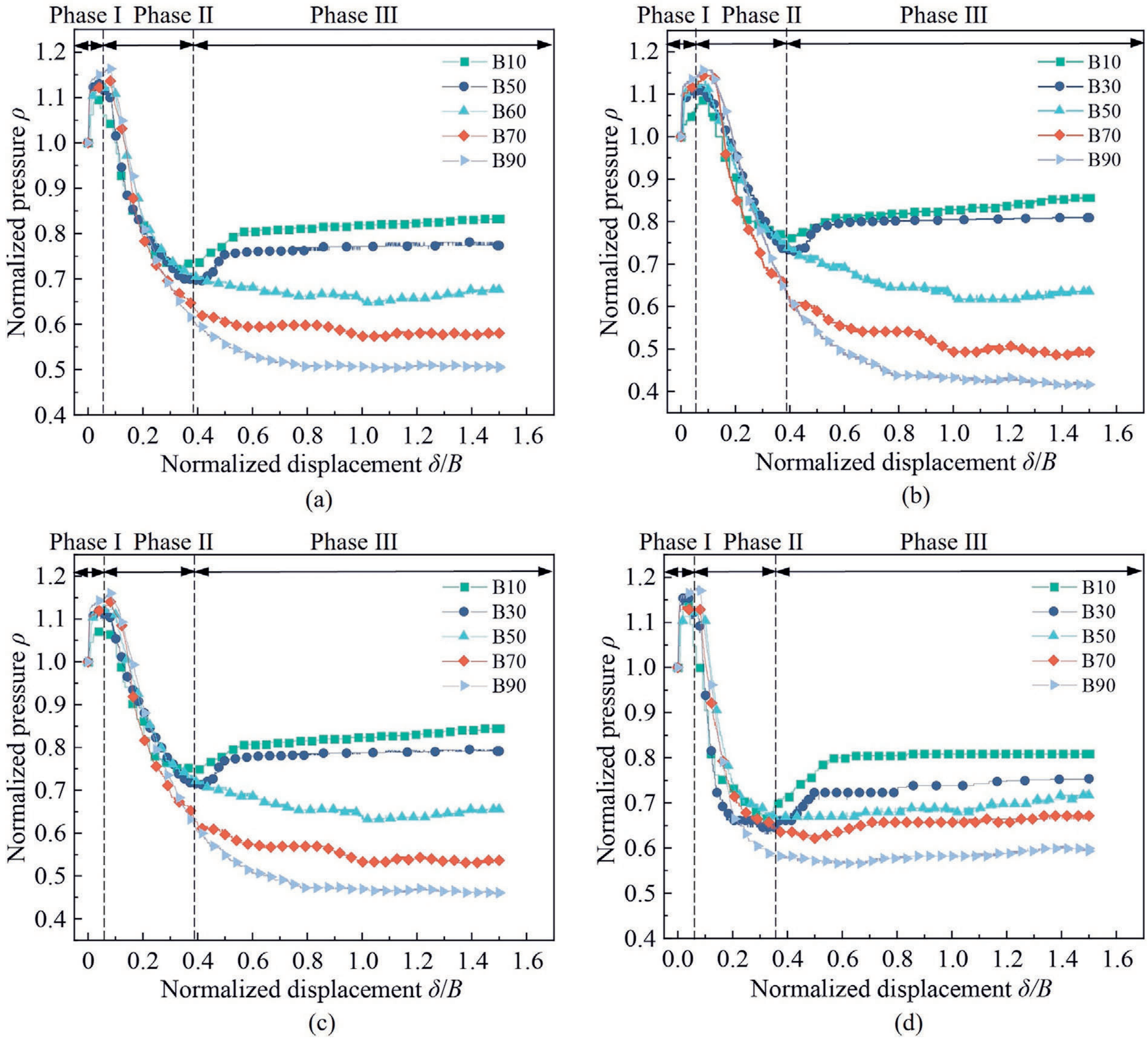

(a) (b) (c) (d)

Fig. 8. Variation in the average normalized pressure on both sides of the trapdoor with displacement. (a) Sensors 21 and 22, (b) Sensors 20 and 23, (c) Sensors 19 and 24, and (d) Sensors 18 and 25.

pressure (soil arching ratio) versus normalized displacement at various positions adjacent to the trapdoor.

To improve measurement accuracy, normalized pressures were obtained by averaging the measurements from sensors symmetrically placed on both sides of the trapdoor. Results indicated that soil pressure adjacent to the trapdoor exhibited three distinct stages as the trapdoor displacement increased: (1) A rapid increase stage, where pressure in the central region quickly decreased as displacement occurred, while the soil arching developed and redirected load toward the side regions. (2) A gradual decrease stage, with continued trapdoor descent, the load propagates further outward, causing the lateral pressures to diminish gradually. (3) A stabilization stage, wherein the soil arching effect eventually stabilized, and lateral pressures consequently reached equilibrium. The pressure response behavior differed significantly between shallow and deep burial conditions across these stages. Under shallow conditions (10, 30 m), lateral pressures recovered following their initial decrease and subsequently stabilized. In contrast, under deeper conditions (50, 70, 90 m), lateral pressures exhibited rapid increases followed by a gradual reduction prior to stabilization, without undergoing a distinct rebound phase.

Based on the identified soil-pressure variation patterns, this study classifies the domain into three distinct regions: as the trapdoor displacement increases, differential movement between the soil above the trapdoor and that on either side causes the overlying soil pressure to decrease and to be transmitted outward, thereby forming a loosened zone and generating a concomitant pressure zone in the flanking soils. With further trapdoor descent, the load within this pressure zone continues to propagate outward and evolves into an unloading zone, while a new pressure zone emerges at a greater distance.

Analysis of the pressure–displacement curves measured at various distances from the trapdoor edge reveals that the unloading zone extends from the trapdoor boundary to approximately 1.2*B*–1.5*B*. Outside the unloading zone, new pressure zones are established, and Fig. 9 presents the relationship between the normalized pressure (soil arching ratio) and normalized displacement specifically within these regions. Again, the normalized pressure values were determined by averaging the readings from symmetrically placed sensors located at identical positions on either side of the trapdoor. Within these pressure zones, soil pressure evolves in two distinct stages: initially, a rapid increase stage, followed by a slower incremental stage.

The pressure evolution within the pressure zones correlates significantly with the stress evolution characteristics observed in the unloading zones, especially during the rapid increase phase. As the trapdoor displacement progresses, stresses from the unloading zone gradually propagate outward into these pressure zones, resulting in an initially rapid increase in their pressure. More precisely, the rapid increase phase in the pressure zone occurs nearly simultaneously with the rapid decrease of pressure in the unloading zone. This indicates that the trapdoor displacement not only directly affects soil pressures within the unloading zone but also progressively transfers these stress changes outward into adjacent pressure zones. As stresses continue to migrate outward, pressure zones gradually absorb increasing loads, causing the rate of pressure increment to diminish over time until a stable equilibrium is eventually attained.

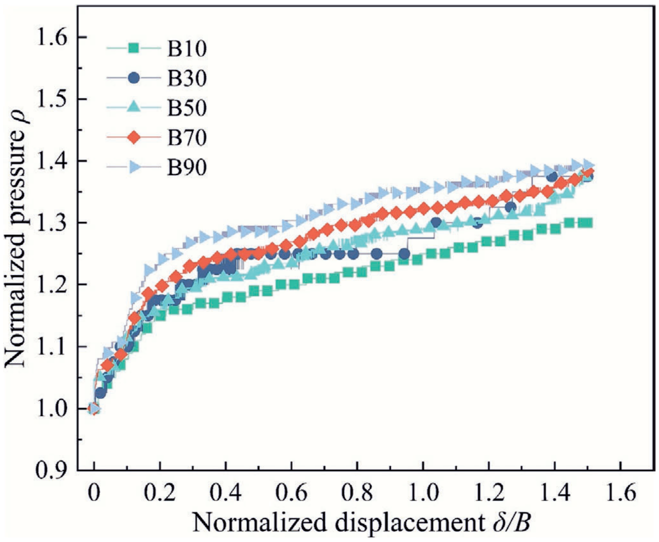

Fig. 9. Variation in the average normalized pressure measured by Sensors 32 and 11 with displacement.

3.3 Characteristics of soil displacement

To investigate the spatial extent and failure mechanisms of soil arching at different burial depths, this chapter employs DIC to obtain soil displacement and strain fields. As a non-contact technique, DIC enables real-time monitoring of soil deformation without disturbance, providing intuitive and quantitative data to elucidate soil arching formation and stress-transfer pathways.

3.3.1 Horizontal displacement of soil

Table 3 presents the evolution of horizontal soil displacement under different burial depths and varying trapdoor descent distances. Under shallow conditions, symmetrical fan-shaped horizontal displacement zones clearly form on both sides of the trapdoor. As the trapdoor descends, the initial displacement zone gradually splits into multiple new zones, which extend upward and gradually expand laterally. With continued zone development, the angle between newly formed zones and the horizontal direction progressively increases. At burial depths of 10 and 30 m, the final heights of these horizontal displacement zones reach 483.3 and 393.1 mm, respectively, while their widths remain around 170 mm for both depths, indicating similar width characteristics.

Under deeper conditions, symmetrical fan-shaped horizontal displacement zones likewise consistently develop on both sides of the trapdoor. Unlike in shallow settings, the newly formed zones maintain the same orientation as the initial zones, continuing to expand upward along the original trajectory and outward to the sides as the trapdoor lowers. This development pattern contrasts markedly with that in shallow conditions, reflecting significant differences in soil stress states and displacement behavior across varying burial depths. At burial depths of 50, 70, and 90 m, the final heights of the horizontal displacement zones measure 306.1, 265.5, and 242.1 mm, respectively, indicating a gradual decrease in zone height with increasing burial depth. At 90 m, the height of the displacement influence is reduced to about 50% of that at 10 m. Nevertheless, in contrast to the varying final heights, the width of the horizontal displacement zone remains consistently around 170 mm across all five tests, suggesting that simulated burial depth has a minimal effect on its width. This observation also aligns with the study's assumption about the width of the unloading zone, further confirming the stability of the unloading zone width under different burial depths.

Table 3
Characteristics of horizontal displacement evolution under different burial depths and trapdoor displacements.

	δ= 20 mm	δ= 40 mm	δ= 70 mm
H= 10 m	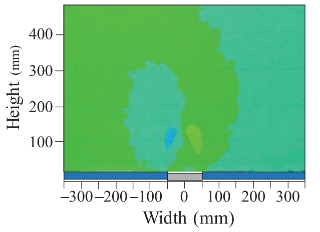	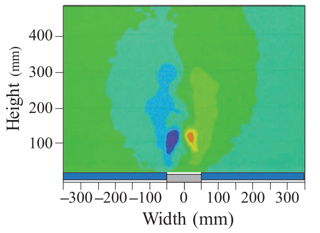	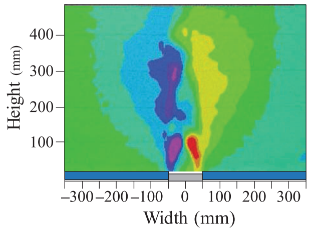
H= 30 m	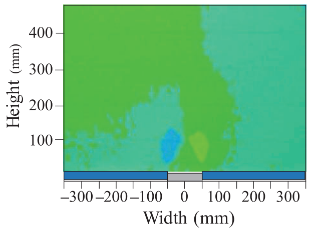	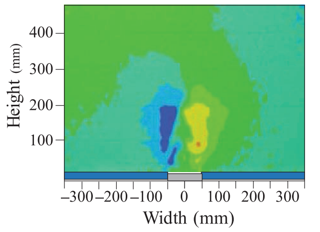	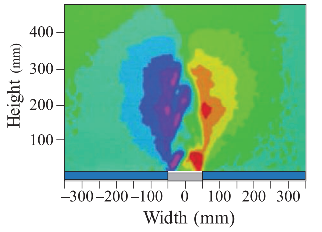
H= 50 m	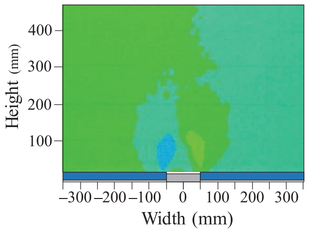	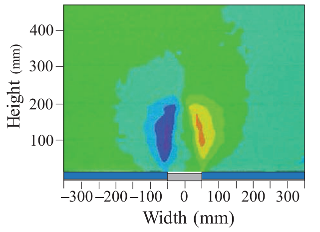	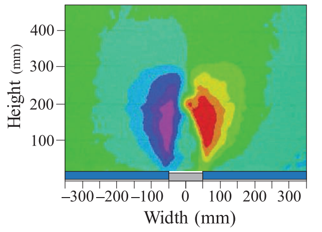
H= 70 m	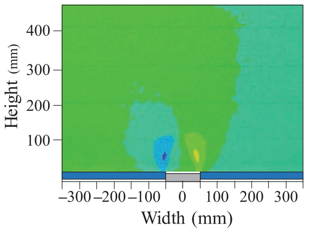	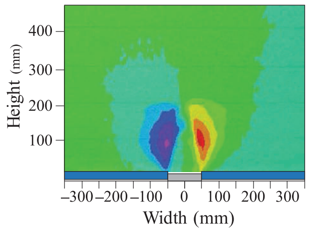	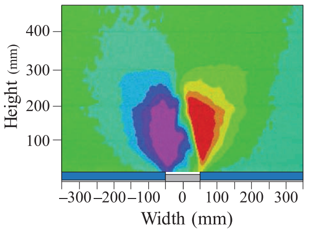
H= 90 m	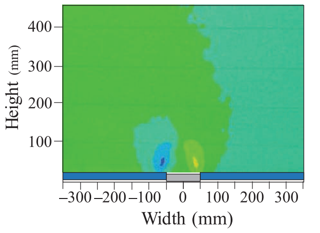	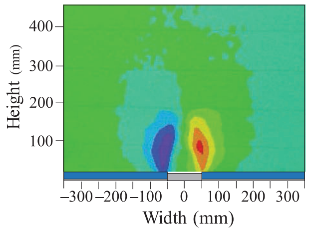	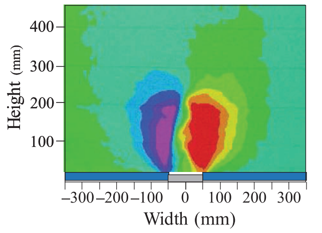
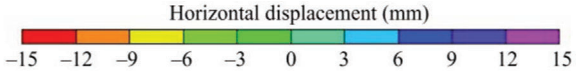			

As illustrated in Fig. 10, the horizontal displacement at a cross-section located 5 mm from the trapdoor surface is plotted against different trapdoor descent distances under varying simulated burial depth conditions. In the initial stage of trapdoor displacement, horizontal deformation occurs only slightly in the immediate vicinity of the trapdoor surface, remaining confined within the trapdoor boundaries. As the trapdoor continues to descend, the magnitude of horizontal displacement increases markedly, and the deformation zone rapidly extends beyond the trapdoor edges, gradually reaching more distant and higher positions, ultimately up to approximately 120 mm from the trapdoor edge. The width of this displacement zone aligns with the unloading zone width specified in Section 3.2 of this study, exhibiting no significant difference across burial depths and indicating that the spatial propagation of horizontal displacement is relatively insensitive to changes in burial depth.

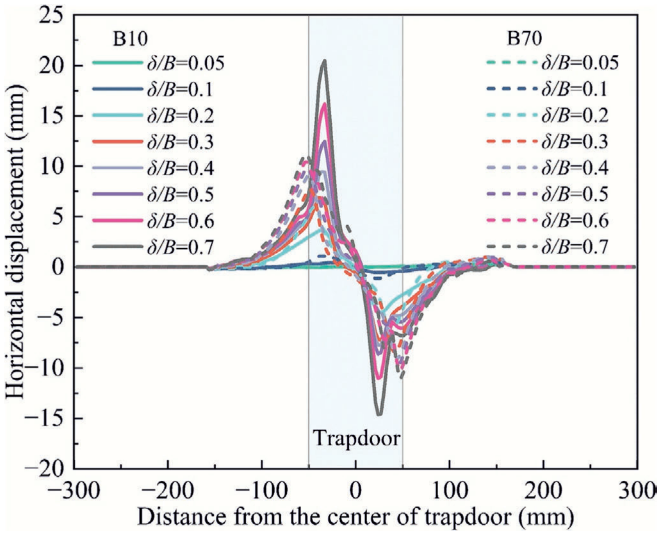

Fig. 10. Comparison of horizontal displacement evolution between 10 and 70 m burial depths.

Nonetheless, while the lateral spread of horizontal displacement appears largely unaffected by burial depth, its magnitude is notably constrained by burial depth: at deeper conditions (70 m), horizontal displacement is substantially smaller during all phases of trapdoor descent compared with shallower conditions (10 m). In addition, under deeper conditions, the peak shear strain zone shifts laterally relative to its location in shallower conditions. The underlying mechanism for this lateral shift will be further clarified in the subsequent analysis of variations in the inclination of shear bands.

As shown in Fig. 11, shallow and deep conditions exhibit markedly distinct development patterns for the horizontal displacement zone. Overall, the mode of horizontal displacement evolution varies markedly with burial depth. Under shallow conditions, as the trapdoor descends, newly formed displacement zones progressively deviate from their

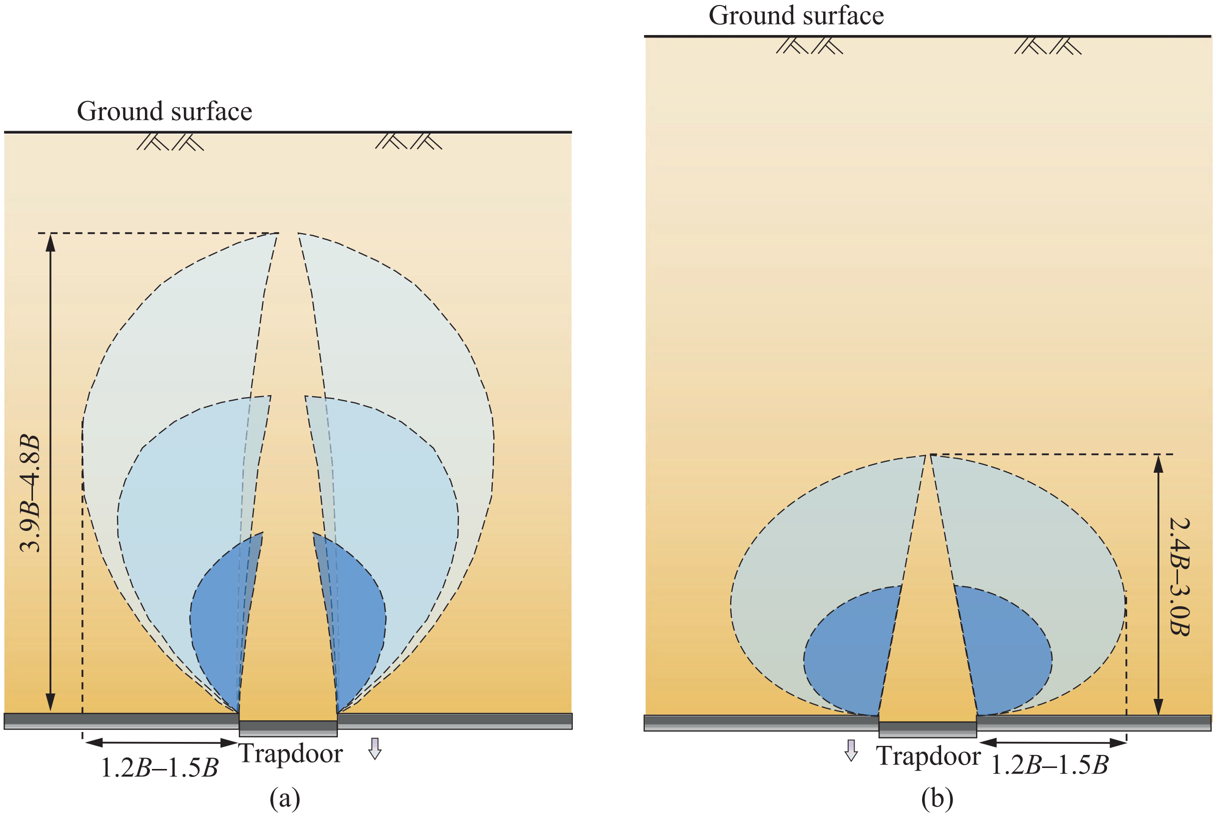

(a) (b)

Fig. 11. Evolution of horizontal displacement patterns. (a) Shallow condition, and (b) deep condition.

original trajectory, ultimately extending to heights of 3.9*B*–4.8*B* and spanning a width of 1.5*B*. In contrast, under deep conditions, the displacement zone continues along its initial path, reaching a final height of 2.4*B*–3.0*B* while also maintaining a 1.5*B* width. The underlying reason for these differences lies in the lower initial stress levels in shallow soils, which foster multiple instances of displacement zone splitting and reconstruction, resulting in greater overall heights. By comparison, the higher vertical stress constraints in deeper soils lead newly formed zones to extend along the original trajectory, resulting in reduced final heights but a more stable overall geometry.

3.3.2 Vertical displacement of soil

Table 4 presents the evolution of vertical soil displacement under different burial depths and various trapdoor descent distances. Changes in vertical displacement play a critical role in revealing the process of soil arching formation, making it an essential indicator of soil behavior and arching characteristics.

Table 4
Characteristics of vertical displacement evolution under different burial depths and trapdoor displacements.

	δ= 20 mm	δ= 40 mm	δ= 70 mm
H= 10 m	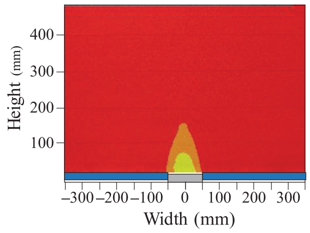	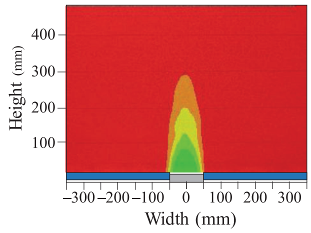	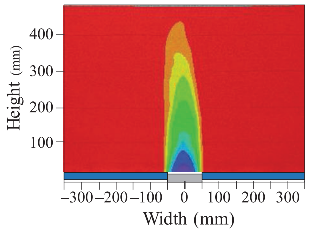
H= 30 m	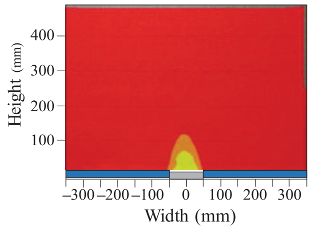	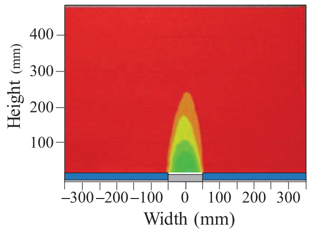	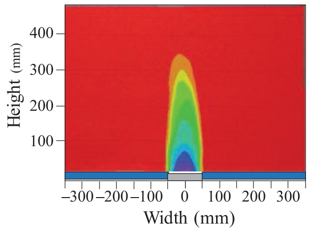
H= 50 m	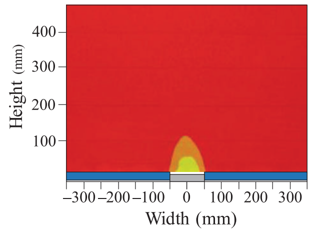	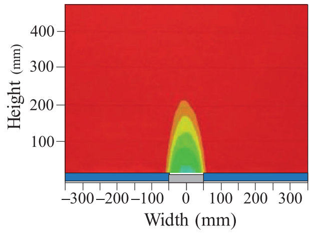	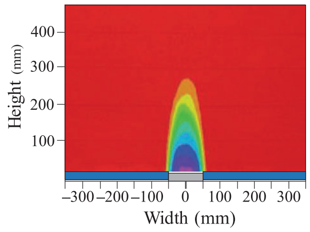
H= 70 m	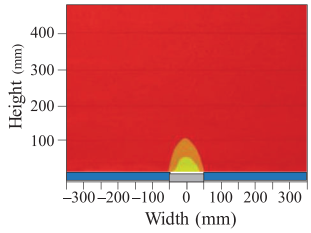	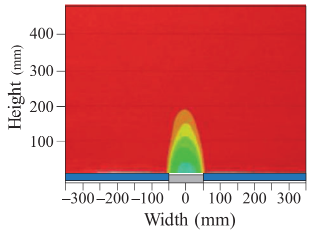	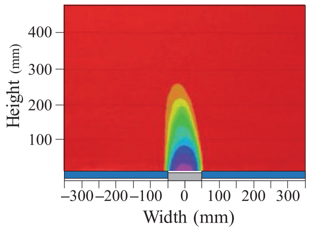
H= 90 m	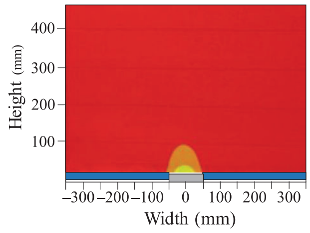	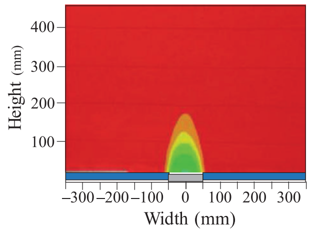	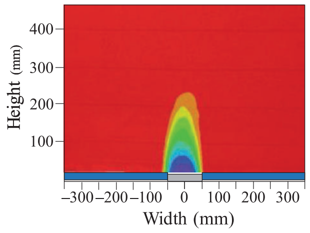
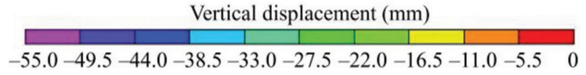			

Under shallow conditions, vertical displacement progresses through three distinct stages. During the initial phase of arching formation, the vertical displacement above the trapdoor exhibits a triangular pattern, with heights of 155.1 and 121.8 mm at burial depths of 10 and 30 m, respectively. As the trapdoor continues to descend, the displacement region transforms into a tower-like shape, extending upward. Eventually, the vertical displacement evolves into a parabolic form and extends further upward. At 10 m and 30 m burial depths, the final heights of vertical displacement reach 436.7 mm and 346.9 mm, respectively. Throughout this process, vertical displacement initially remains confined within the trapdoor boundaries before gradually extending slightly beyond the trapdoor width. In contrast to the shallow condition, vertical displacement under deeper burial conditions follows a parabolic pattern from the onset of arching formation, measuring initial heights of 112.6, 107.1, and 98.3 mm at burial depths of 50, 70, and 90 m, respectively. As the trapdoor descends further, the parabolic pattern of vertical displacement persists, but develops more gradually than under shallow conditions.

This distinctly different pattern underscores the significant variations in arching evolution between shallow and deep conditions. At 50, 70, and 90 m burial depths, the final vertical displacement heights reach 272.5, 253.6, and 230.8 mm, respectively. Importantly, despite the varying final heights, the width of the vertical displacement remains similar to that observed under shallow conditions, indicating a relatively stable displacement zone width across different burial depths. Therefore, the evolution of vertical displacement under different burial depths exhibits marked differences. Under shallow conditions, vertical displacement proceeds through multiple stages-triangular, tower-like, and parabolic-whereas deeper conditions predominantly show a single parabolic development pattern. As burial depth increases, the maximum vertical displacement height gradually decreases, particularly evident in shallow conditions. By contrast, the displacement width remains relatively stable across different burial depths.

To further quantify this difference, the “loosening zone height” in this study is defined as the elevation at which the vertical displacement decreases to 10% of its maximum value at the stage of peak soil arching. As shown in Fig. 12, taking the 90 m simulated burial depth as an example, extract vertical displacement data along section AA' to calculate the height of the loosening zone. Based on this criterion, the loosening zone heights under different burial depths were determined to be 152.3, 129.1, 114.2, 105.4, and 98.3 mm, respectively. The results indicate a gradual reduction in loosening zone height with increasing burial depth, reflecting the more constrained vertical deformation characteristics under deeper conditions. These vertical displacement characteristics further demonstrate that, as the trapdoor gradually descends, the soil directly above it becomes loosened, begins to displace, and progressively forms a soil arching. However, differences in the soil's confining capacity under various burial depths lead to repeated fracturing and reconstruction in shallow layers, culminating in a multi–stage evolution of vertical displacement. This phenomenon contrasts sharply with the relatively steady evolution observed under deeper conditions. Throughout this process, shifts in vertical displacement dynamics directly affect horizontal displacement evolution, thereby accentuating the distinctions in overall displacement behavior between shallow and deep conditions.

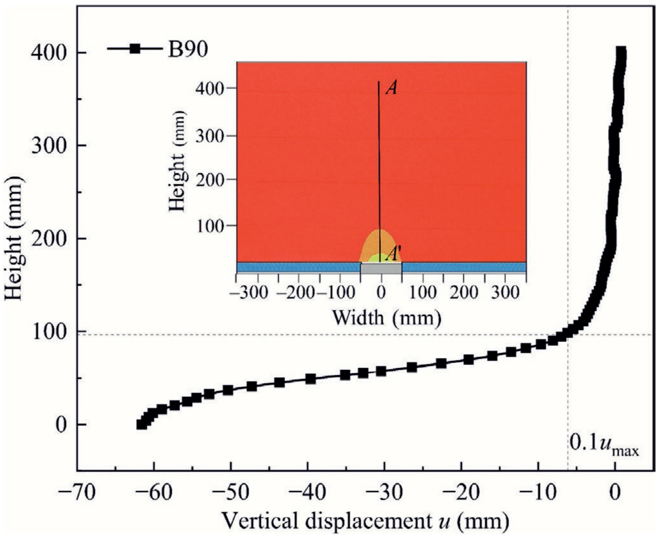

Fig. 12. Schematic illustration of loosening zone height determination.

Figure 13 illustrates the different evolution patterns of vertical displacement. Under varying burial depths, soil arching development exhibits pronounced disparities. In shallow conditions, vertical displacement undergoes three stages: initially forming a triangular pattern, transitioning into a tower-like shape, and ultimately evolving into a parabolic pattern, reaching a final height of approximately $3.5B$ to $4.3B$. In contrast, vertical displacement under deep conditions maintains a consistent parabolic pattern throughout trapdoor descent and reaches a final height of approximately $2.2B$ to $2.7B$. Furthermore, regardless of burial depth, when the trapdoor displacement is relatively small, vertical displacement remains confined within the trapdoor width. As displacement increases, vertical displacement progressively extends beyond the trapdoor boundaries.

Figure 14 shows the vertical displacement of the soil at a cross-section 5 mm above the trapdoor, for burial depths of 10 and 70 m. The data are plotted against the downward displacement of the trapdoor. When the trapdoor displacement is relatively small, vertical displacement occurs only slightly near the center of the trapdoor, remaining largely confined within its boundaries. As the trapdoor descends further, the vertical displacement increases in magnitude and extends slightly beyond the trapdoor's edges, slightly exceeding the trapdoor's edges, though the peak displacement remains near the trapdoor center throughout. Moreover, different burial depths markedly affect the magnitude

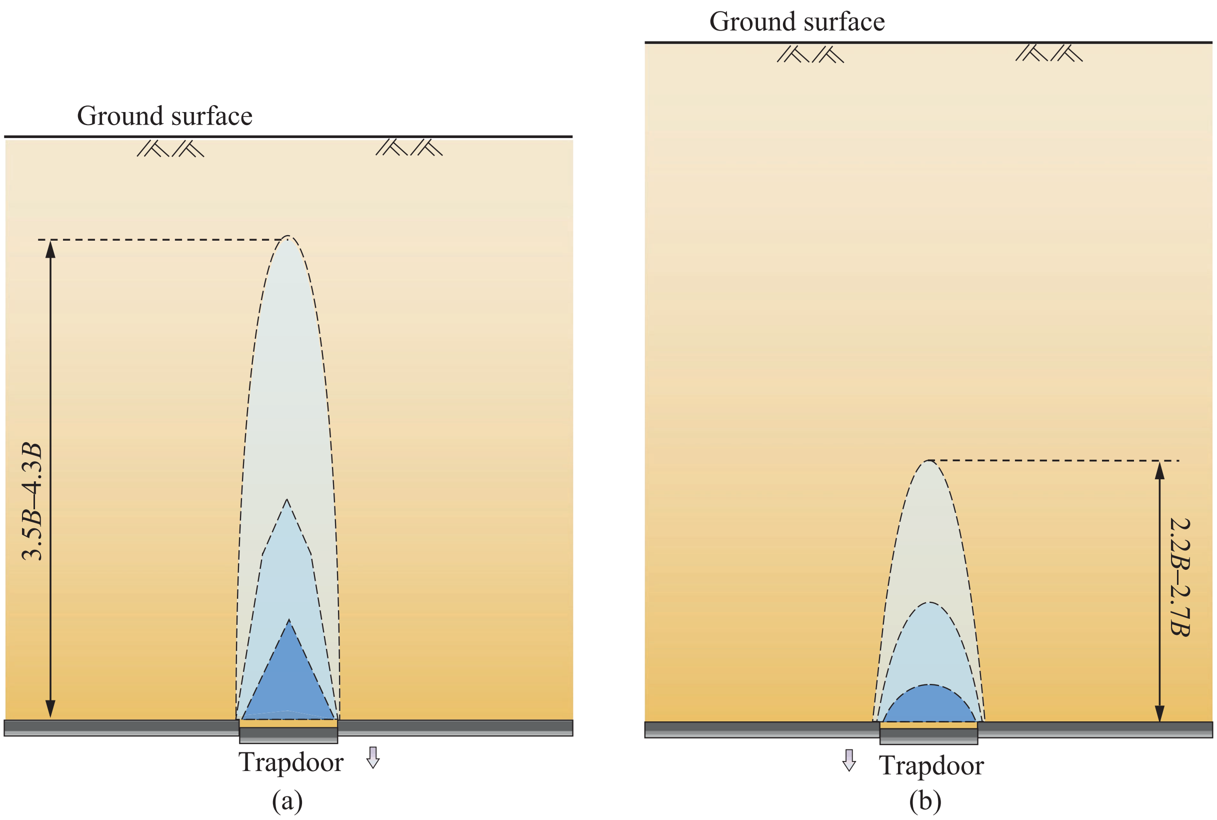

Fig. 13. Evolution of vertical displacement patterns. (a) Shallow condition, and (b) deep condition.

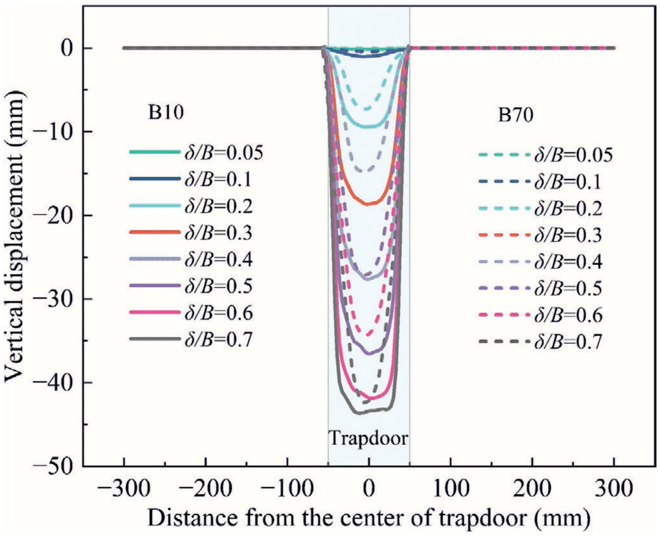

Fig. 14. Comparison of vertical displacement evolution between 10 m and 70 m burial depths.

of soil displacement: compared with the shallow condition (10 m), vertical displacement under deeper conditions (70 m) is noticeably smaller at every stage of trapdoor descent, indicating that increasing burial depth exerts a pronounced inhibitory effect on vertical deformation.

At different stages of trapdoor displacement, Fig. 15 illustrates how the height of vertical displacement influence (d_h) varies with burial depth. Under shallow conditions, burial depth exerts a significant impact on the influence height, whereas under deep conditions, this effect gradually weakens. With increasing burial depth, trapdoor-induced vertical displacement in the overlying soil decreases significantly. This suggests that increased burial depth enhances the development of the soil arching effect. Once the soil arching forms and stabilizes, part of the overburden pressure is redistributed to deeper or more distant soil regions, thereby limiting vertical deformation immediately above the trapdoor.

3.4 Shear strain and shear band

A detailed and systematic investigation of soil arching based on shear strain analysis clarifies not only the soil deformation behavior but also the associated shear strength characteristics. It further provides valuable and nuanced insights into displacement patterns, arching formation processes, and the corresponding failure mechanisms. Table 5 outlines in detail the evolution of shear strain with increasing trapdoor displacement under various burial depths. The results indicate that when the trapdoor descends to approximately 20 mm, two shear bands initially emerge at the edges on both sides of the trapdoor. As the displacement further increases, the development of shear bands exhibits pronounced differences under varying burial depths: under shallow burial, the two initially

Table 5
Characteristics of shear strain evolution under different burial depths and trapdoor displacements.

	δ= 20 mm	δ= 40 mm	δ= 70 mm
H = 10 m	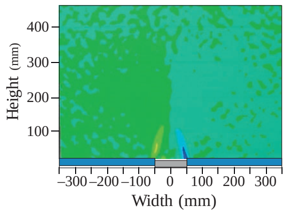	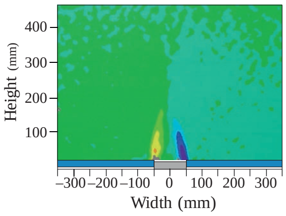	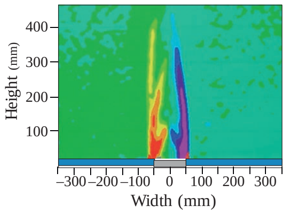
H = 30 m	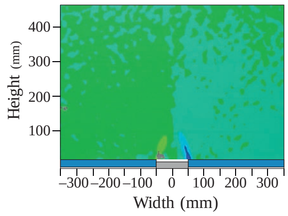	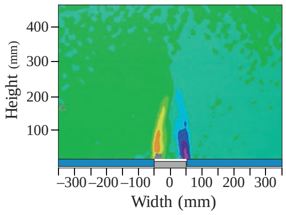	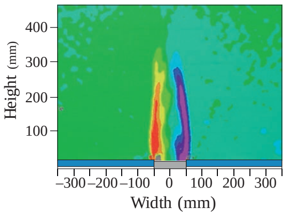
H = 50 m	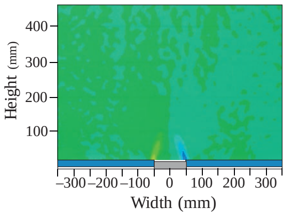	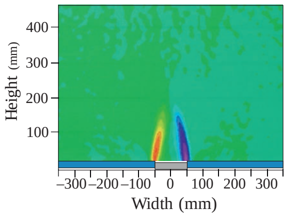	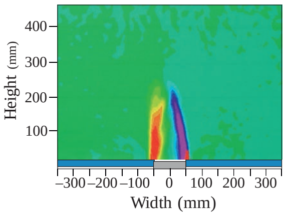
H = 70 m	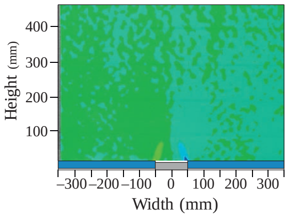	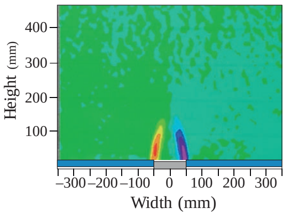	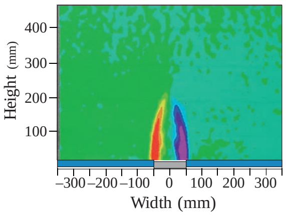
H = 90 m	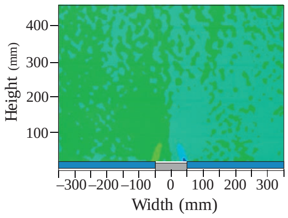	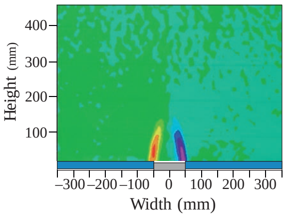	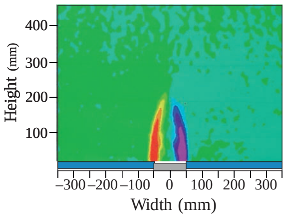
Shear strain e_{xy} (%) −45 −36 −27 −18 −9 0 9 18 27 36 45			

formed shear bands progressively converge toward the center and a new shear band develops above; whereas under deep burial, only a single dominant shear band is observed, and its morphology also shows a tendency toward closure. Moreover, the final heights of the shear bands vary significantly with burial depth, measuring 431.6, 338.9, 251.6, 218.9, and 210.3 mm at 10, 30, 50, 70, and 90 m, respectively. This trend indicates that greater burial depth substantially limits shear band development, resulting in reduced final heights. This phenomenon likely results from the increased confining pressure at greater depths, which inhibits the upward propagation of shear bands. It highlights the greater complexity of deformation behavior in deep soil layers.

Figure 16 illustrates the detailed evolution of the shear band inclination angle (α) with increasing trapdoor displacement at different burial depths. The inclination angle of the shear band was determined based on quantitative measurements of the DIC-derived shear strain field. Specifically, peak shear strain points were extracted at two horizontal cross-sections, $y = 0$ mm and $y = 100$ mm, and the angle was calculated by connecting these two points. This approach, which provides an estimate of the overall inclination angle, has also been adopted in previous studies such as Zhao et al. (2021). When the shear band had not yet developed up to $y = 100$ mm, the peak shear strain at $y = 50$ mm was used as a substitute.

To further verify the robustness of this approach, this study additionally analyzes the shear band by dividing it into multiple vertical intervals, each 30 mm in height (as shown in Fig. 16). In each interval, a linear fit was performed through the local peak strain points to determine the inclination angle at that specific height. The results, presented in Fig. 16, illustrate the variation of shear band inclination with height under different burial depths when the trapdoor displacement reaches 70 mm. The findings indicate that under shallow burial conditions, the local inclination angles below 120 mm are generally consistent with the overall inclination angle. Similarly, for deep burial conditions, the local inclination angles below 90 mm show good agreement with the overall inclination, demonstrating that the two-point method provides a reasonable representation of the shear band orientation. Moreover, under shallow burial, the inclination angle exhibits minimal variation in the 120–210 mm height range, which can be attributed to the gradual closure of the initial shear band and the upward propagation of a newly formed band. In contrast, under deep burial, the shear band does not fully close; rather, the initial band gradually converges, leading to a noticeable reduction in inclination angle between 90–210 mm. These patterns are not artifacts of DIC measurement noise but rather reflect the inherent mechanisms of soil arching induced by trapdoor movement.

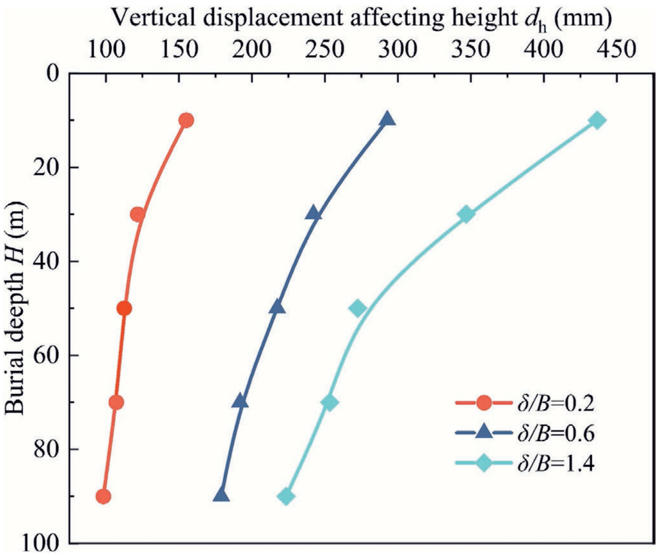

Fig. 15. Variation of the vertical displacement affecting height with burial depth.

As shown in Fig. 17, at the same burial depth, the inclination angle between the shear band and the horizontal direction increases with greater trapdoor displacement. This trend is primarily attributed to the deformation of the soil mass triggered by the trapdoor movement, which leads to a reduction in confining pressure near the trapdoor and consequently increases soil dilatancy, manifested as a gradual increase in shear band inclination. A more comprehensive examination across varying burial depths indicates that the shear band angle gradually decreases with increasing burial depth, suggesting that deeper layers—with higher overall strength and greater confining pressure—tend to produce more gently sloping shear bands.

In such deep-layer conditions, the soil experiences a localized shear with minimal deformation with reduced dilatancy, enabling the soil arching to remain intact for a longer duration. Consistent with the present findings, Rui et al. (2024) similarly observed the development of two symmetric sliding surfaces originating at the trapdoor edges in both 2D and 3D trapdoor tests, whose inclination angles relative to the horizontal (complementary to the angle measured in this study) increased with normalized displacement. Moreover, backfill with higher relative den-

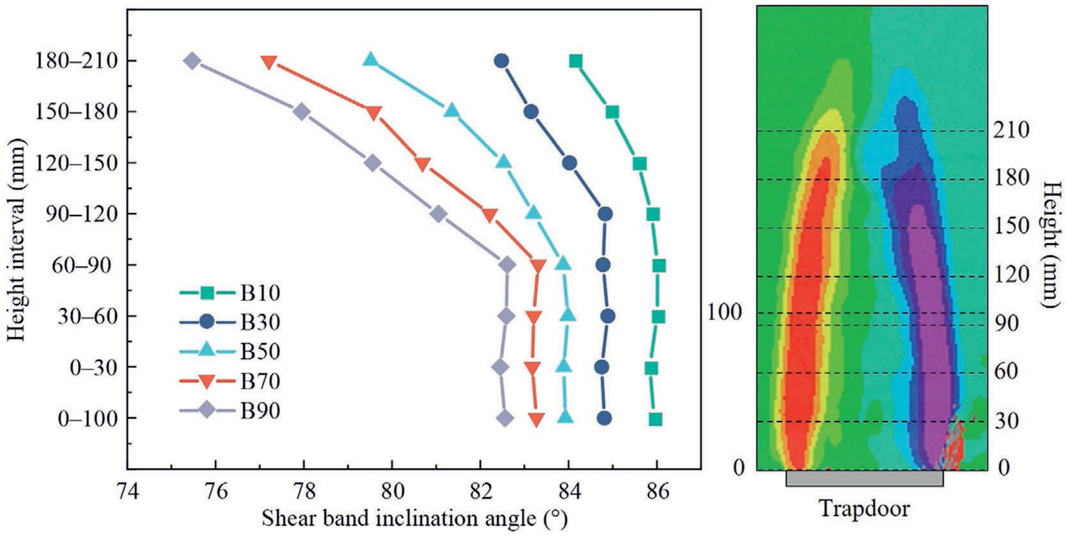

Fig. 16. Variation of shear band inclination across different height intervals under various burial depths.

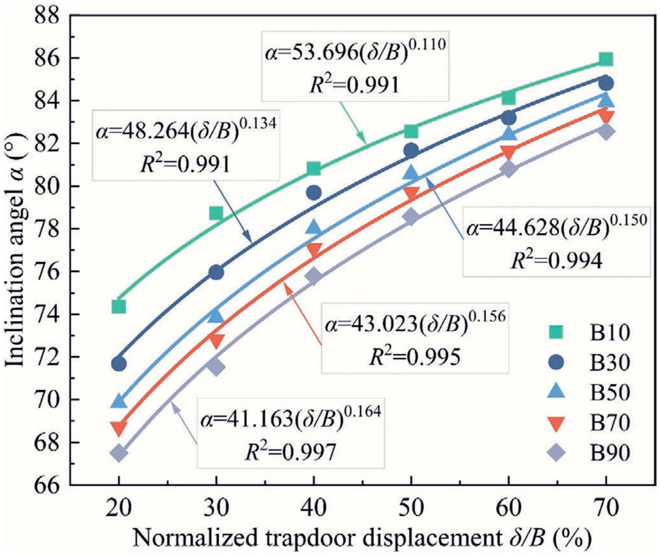

Fig. 17. Variation in the shear band inclination angle with trapdoor displacement.

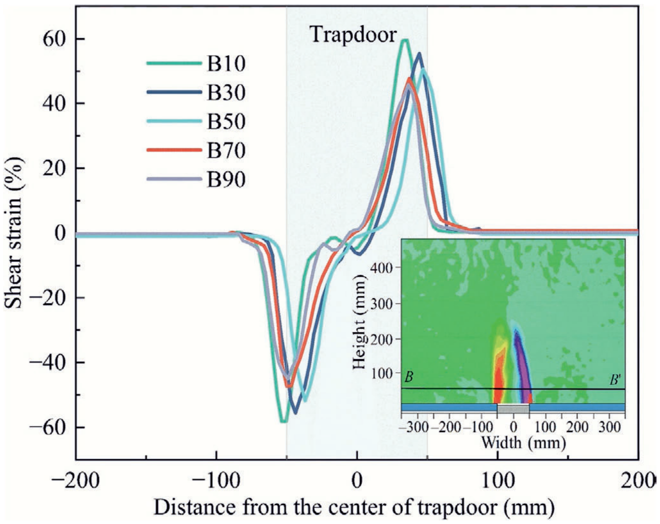

Fig. 18. Shear strain analysis at a 30 mm trapdoor, taking the 50 m simulated burial depth as an example.

sity exhibited larger initial inclination angles, consistent with the trend in shear band angles seen under different burial depths in the present experiments.

To further investigate shear strain evolution during soil failure, the spatial distribution of shear bands under shallow and deep conditions is examined. As shown in Fig. 18, a horizontal cross-section, *BB*', located 50 mm above the trapdoor was selected, and the variation of shear strain along this section was captured using VIC-2D software. For comparison purposes, the same section position was selected under different burial depth conditions. It is worth noting that the VIC-2D program sets the origin of the Cartesian coordinate system at the geometric center of the area of interest (AOI), leading to negative shear strain on the left side. Experimental results reveal that, under all test conditions, the maximum shear strain occurs at the edges of the trapdoor. This finding indicates that the edges of the soil layer serve as the starting point of shear failure, playing a pivotal role throughout the failure process. Furthermore, the maximum shear strain gradually decreases with increasing burial depth, suggesting that higher confining pressure in deeper layers constrains shear band development. Detailed analysis of shear strain distribution at various positions confirms that values peak near the trapdoor and decline sharply, stabilizing as they extend beyond the arching influence zone. This trend underscores the significant impact of soil arching on the spatial distribution and evolution of shear strain.

The thickness of shear bands in granular materials generally depends on factors including stress level, relative density, particle size and shape, dilation and internal friction angles, confining pressure, loading conditions, geometry, and boundary conditions (Alshibli & Hasan, 2008; Guo, 2012; Lade, 2003; Vermeer, 1990). The shear band boundaries are commonly defined where the shear strain reaches 50% of the maximum shear strain in the profile, as illustrated in Fig. 19. To quantitatively analyze the variation of shear band thickness with burial depth and trapdoor displacement, a horizontal cross-section, *CC*', located 50 mm above the trapdoor, was selected. Given the presence of a certain inclination in the shear band, trigonometric functions were employed to calculate the thickness in the direction perpendicular to the shear band, and the average thickness (t) of the left and right shear bands was taken as the representative value.

The thickness of the shear band is typically normalized by the median particle size (d_{50}). Figure 20 illustrates the quantitative relationship between normalized trapdoor displacement and normalized shear band thickness under different burial depths. The maximum normalized shear band thickness in this study is approximately 120, which is slightly larger than the range (34–107) reported by Costa et al. (2009). However, considering factors such as the magnitude of trapdoor displacement, relative density, and loading method, the measured thickness in this study remains within a reasonable range. Experimental results reveal that as the trapdoor displacement increases, the soil undergoes progressive shear deformation, resulting in continuous outward extension of the shear band and an increase in its thickness. However, burial depth has no significant effect on the thickness of the shear band.

3.5 Classification criteria for shallow and deep burial conditions

Based on the observed differences in soil pressure distribution, displacement characteristics, and arching mechanisms detailed in previous sections (3.1–3.4), a classification criterion for shallow and deep soil layers can be clearly established. This section systematically analyzes the influence of burial depth on the soil arching effect

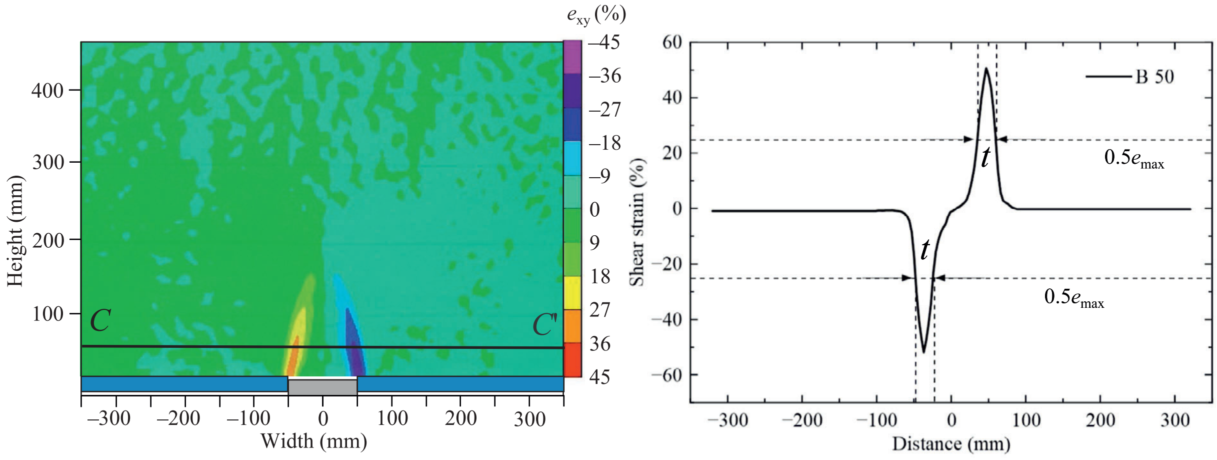

(a) (b)

Fig. 19. Illustration of shear band thickness extraction, taking the 50 m simulated burial depth case at a trapdoor displacement of 30 mm as an example. (a) 50 m simulated burial depth case at a trapdoor displacement of 30 mm, and (b) illustration of shear band thickness extraction.

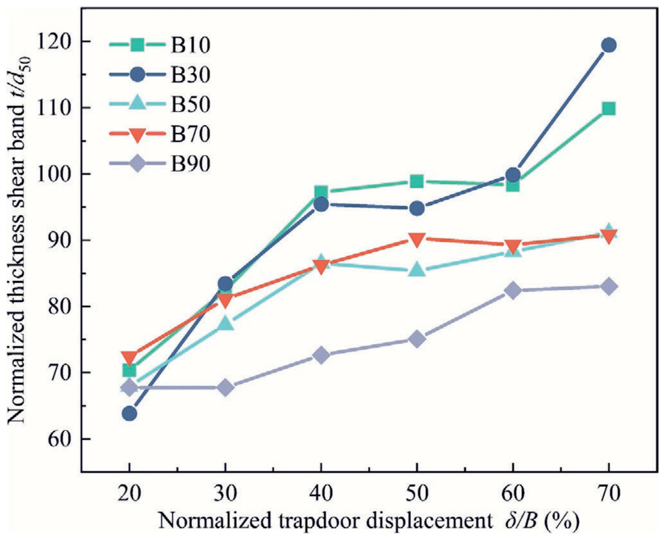

Fig. 20. Variation in shear band thickness with trapdoor displacement.

through examining the displacement-load relationship curves, horizontal displacement characteristics, and vertical displacement characteristics.

Figure 21 compares these factors under 10 m (Fig. 21(a)) and 70 m (Fig. 21(b)) burial depths. The test results reveal that, for shallow soils, the GRC during failure can be divided into three stages: (1) a marked stress reduction stage, (2) a recovery stage, and (3) a stabilization stage. Correspondingly, multiple horizontal displacement bands (Fig. 11(a)) form within the soil, while vertical displacement progresses through triangular, tower-like, and parabolic patterns (Fig. 13(a)). By contrast, under deep soil conditions, the GRC exhibits only two distinct stages: (1) an initial marked stress reduction followed directly by (2) a stable stage without any intermediate recovery. In this scenario, only one pair of horizontal displacement bands (Fig. 11(b)) develops, and vertical displacement follows a parabolic pattern (Fig. 13(b)) until the end of the failure process.

Based on the analysis of soil arch ratios (Fig. 22) at different stages of trapdoor displacement and various burial depths, a clear pattern emerges: in shallow soils, the minimum soil arching ratio decreases significantly with increasing depth, whereas in deeper soils, it remains nearly unchanged and essentially stable. This trend suggests that, once soil failure occurs in deeper strata, the abrupt drop in pressure within the failure zone gradually levels off, reflecting a more stable soil arching effect at greater depths. Drawing on the GRC, soil arching ratio evolution, and contrasting failure mechanisms of shallow and deep ground, this study proposes the following depth classification for urban underground space: burial depths of less than 50 m are defined as shallow, while those of 50 m or greater are considered deep. However, the threshold between 30 m and 50 m should be interpreted as a critical stress level specific to the tested sand and its relative density, rather than a universally applicable depth value. This division does not account for key engineering factors such as soil type or groundwater conditions. Accordingly, the classification criterion has been reformulated in terms of stress levels rather than depth alone. For the sand used in this study with a minimum and maximum dry density of 1.29 and 1.72 g/cm^3, respectively, and a relative compaction of approximately 80% a rigid loading plate applying an equivalent overburden load of 384 kN generates an average vertical stress of about 800 kPa at the base of the model chamber, corresponding to an equivalent simulated burial depth of approximately 50 m. Based on this, we propose the following classification: vertical stress levels of 0–479 kPa are associated with shallow strata, whereas 800 kPa and above correspond to deep strata.

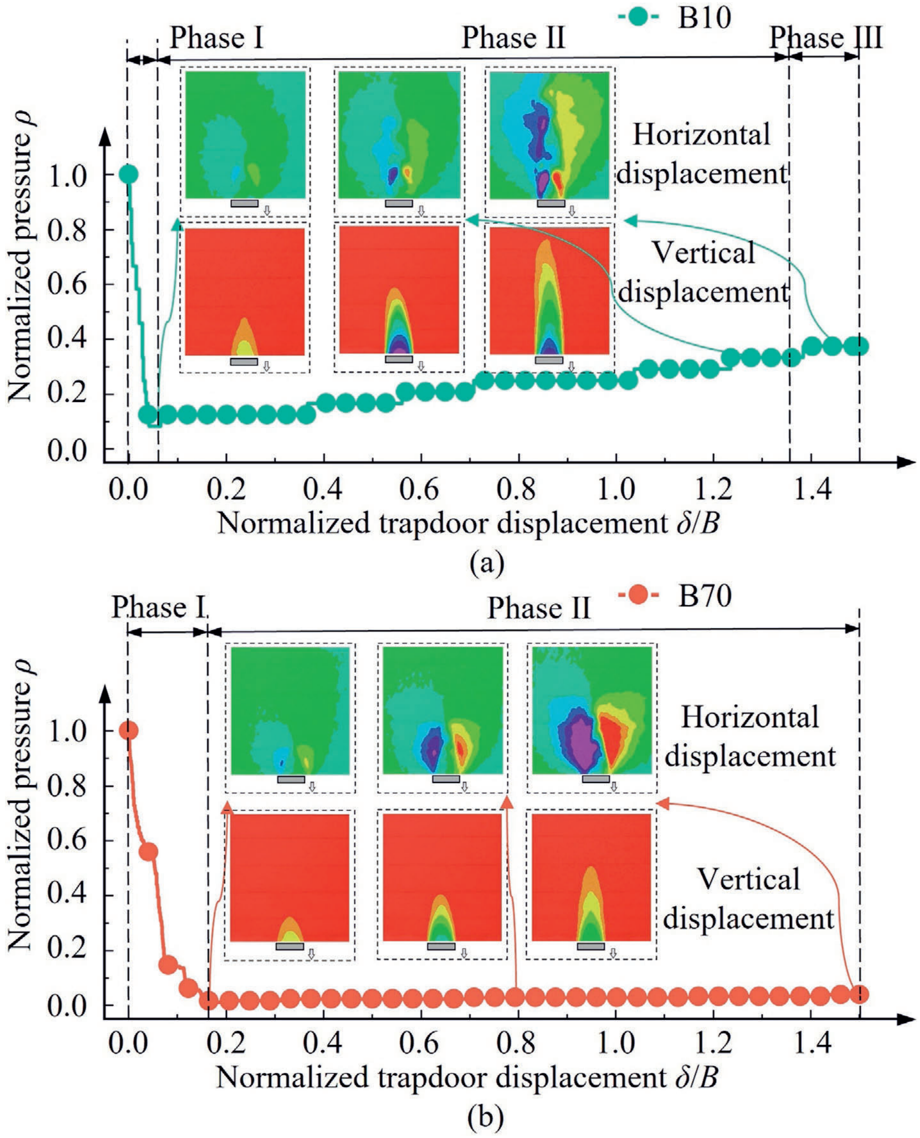

Fig. 21. Typical experimental results under shalldow and deep conditions. (a) Shallow (10 m), and (b) deep (70 m).

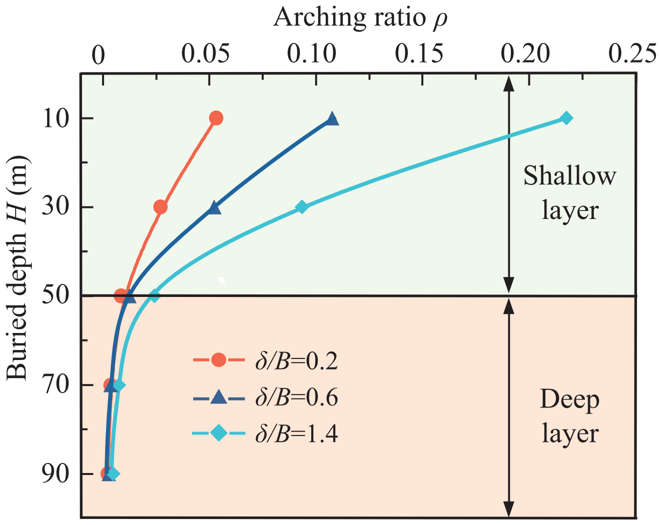

Fig. 22. Classification criteria for shallow and deep burial conditions.

It should be noted that the experimental program was limited to five discrete burial depths: 10, 30, 50, 70, and 90 m. The relatively wide spacing between these depths constrains our ability to characterize the transitional behavior between 30 m (≈479 kPa) and 50 m (≈800 kPa). Therefore, the proposed shallow–deep division should be regarded as an approximate range rather than a strict boundary. Nevertheless, the identified stress threshold offers a valuable reference for stratification in future research on soil arching and can inform the planning, support design, and risk assessment of deep-buried underground structures. Future work will aim to: (1) conduct more densely spaced tests across the shallow–deep transition zone to capture the continuous evolution of soil arching mechanisms; (2) employ numerical simulations (e.g., finite element method (FEM) / discrete element method (DEM) coupling) to validate the criterion under varying confining pressures and soil types; and (3) incorporate complex factors such as seepage and structural interaction to further extend the engineering applicability of this classification framework.

3.6 Soil arching evolution under different burial depths

This section demonstrates the contrasting dynamic evolution patterns of soil arching under shallow and deep conditions by integrating displacement–load relationships with corresponding soil deformation characteristics. As shown in Fig. 23, this integration provides insight into the dynamic evolution of soil arches under varying burial depths. This provides a comprehensive depiction of the evolutionary patterns and distinguishing features of soil arching structures under different burial depths. As illustrated in Fig. 23(a), (1) Maximum soil arching stage: As the trapdoor begins to descend, the vertical stress in the overlying soil drops sharply, resulting in the formation of a loosened zone (Fig. 7, 10–30 m) adjacent to a pressure zone (Fig. 8, Phase I). A closed shear band of notable thickness forms rapidly at their interface, separated by a pair of symmetric shear bands with considerable thickness. (2) Transitional stage: As the trapdoor descends further, the load within the pressure zone spreads outward (Fig. 8, Phase II), while the loosened zone expands markedly upward. This triggers a reloading of the pressure zone (Fig. 8, Phase III), leading to the development of an unloading zone and a new, more distant pressure zone (Fig. 9, 10–30 m). During this process, new upward-propagating shear bands emerge, while the initial shear bands progressively converge and close. (3) Stable stage: continued upward growth of the loosened zone drives further expansion of both the pressure and unloading zones. Simultaneously, the shear band height increases, and the initial shear band eventually forms a fully enclosed loop. Throughout this process, the soil arching undergoes failure and reconstruction before reaching a stable configuration, highlighting the pronounced dynamic nature of soil arching under shallow conditions, multiple episodes of degradation and reformation that ultimately consolidate into a stable load bearing structure.

Compared with the shallow condition, soil arching evolution under deeper conditions exhibits significantly distinct characteristics (Fig. 23(b)). (1) Maximum soil arching stage: Owing to the high initial stress level in deep strata, even a slight descent of the trapdoor causes a sharp reduction in vertical stress, forming a loosened zone (Fig. 7, 50–90 m) bounded by pressure zones on both sides (Fig. 8, Phase I). However, the shear bands that form at the interface are of limited height. (2) Transitional stage: As the trapdoor continues to descend, the upward growth of the loosened zone is much less pronounced than under shallow conditions (Fig. 12). The pressure zones expand laterally and evolve into unloading zones (Fig. 8, Phase

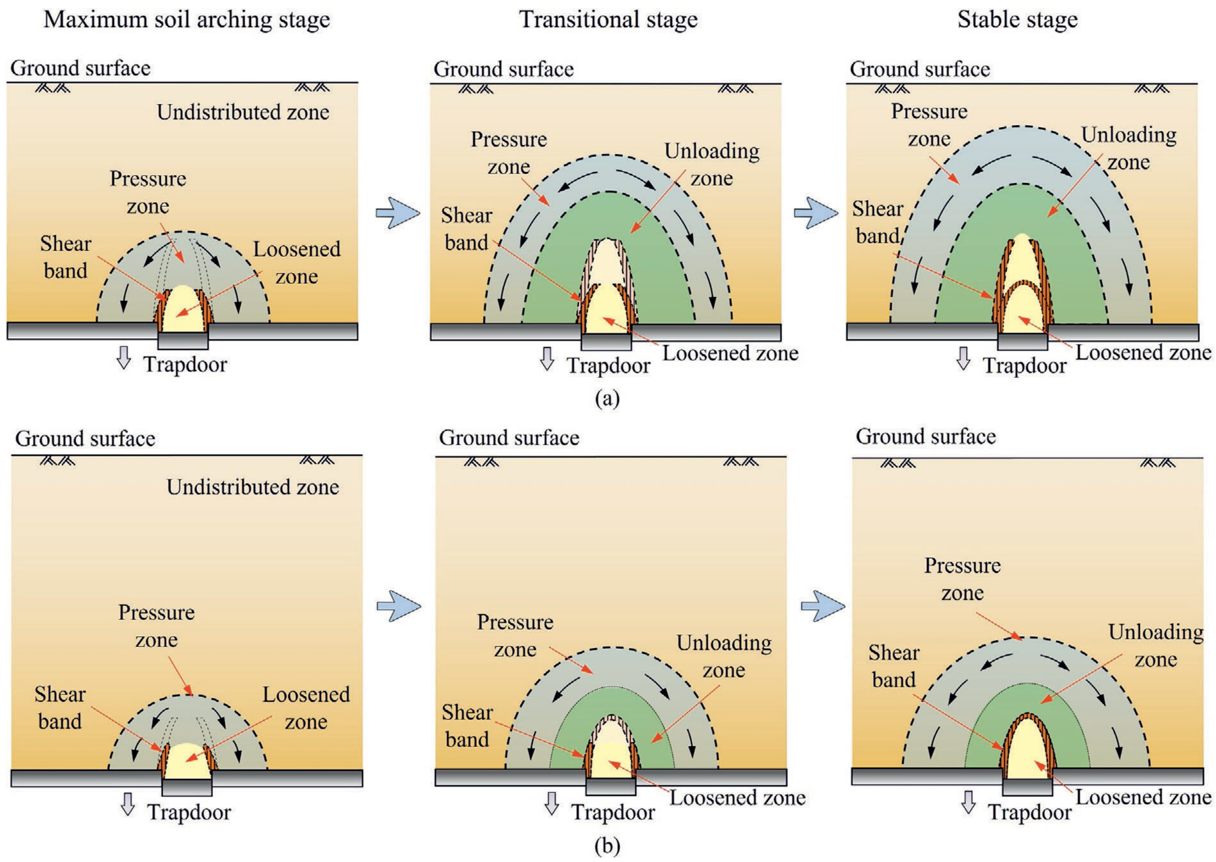

Fig. 23. Dynamic evolution process of soil arching at different stages. (a) Shallow condition, and (b) deep condition.

II–III), while a new, more distant pressure zone gradually forms (Fig. 9, 50–90 m). However, the upward propagation of both the loosened zone and the shear band remains limited. The inclination angle at the shear band tips gradually decreases, exhibiting a tendency toward closure. (3) Stable stage, the shear bands eventually form a closed loop, though their height remains substantially smaller than in shallow cases. As a result, the associated loosened zone is also notably reduced in vertical extent. The displacement-load curves further reveal that, under deep conditions, the soil arching structure reaches stability more rapidly, demonstrating that increasing burial depth markedly strengthens the confining effect of the surrounding soil and thereby enhances the overall stability of the soil arching system.

4 Limitations and future work

This study was conducted under controlled and standardized experimental conditions, allowing for a clear investigation of the fundamental mechanisms of soil arching under extreme high geostress. However, certain simplifications were necessarily made in the experimental setup relative to the complexity of real-world conditions. First, only a single type of sand with a relative density of 80% was used, and all tests were performed under dry conditions. As such, the influences of varying soil types, moisture contents, and groundwater conditions remain unaddressed. Second, the physical model was constrained to two-dimensional plane strain conditions, which do not capture the potential three-dimensional effects present in actual engineering scenarios. Third, the experiments did not consider the effects of reinforcement or structural elements, which often play a critical role in underground construction.

Future work will systematically explore how soil type, saturation, and structural inclusions influence the evolution of soil arching under extreme conditions. In parallel, we plan to conduct multiscale numerical simulations by integrating DEM and FEM, enabling complementary validation with physical tests. Upcoming experimental programs will also incorporate reinforcement materials and structural units to enhance the engineering relevance and theoretical depth of the findings, ultimately aiming to provide more comprehensive scientific support for analyzing soil arching behavior in complex underground environments.

5 Conclusions

This study systematically investigates the dynamic evolution and deformation mechanisms of soil arching across varying burial depths using a self-developed trapdoor apparatus capable of simulating extreme ground failure conditions. The findings highlight the decisive role of burial depth in governing arching formation, stability, and failure modes. Key insights are as follows:

(1) Arching formation and load response: Shallow conditions, arching undergo multiple cycles of arching failure and reformation, reflected in three-stage GRC stress reduction, rebound, stabilization, whereas deep conditions produce a single rapid transition and persistent arching stability, with GRC showing only two stages: pressure drop and equilibrium.
(2) Soil pressure redistribution adjacent to the trapdoor: Shallow conditions show complex stress redistribution increase–decrease–increase–stabilize, indicating periodic arching degradation. Deep conditions exhibit a simple ‘‘monotonic increase–stabilize’’ pattern, reflecting stronger confinement and less degradation.
(3) Horizontal and vertical displacement pattern: Under shallow conditions, horizontal displacement bands evolve as multiple fan-shaped zones, and vertical displacements shift from triangular to tower-like to parabolic profiles. Deep conditions produce lower horizontal bands along initial trajectories, and vertical displacements remain parabolic, reflecting more localized and stable deformation.
(4) Shear band propagation: Shear bands always initiate at the trapdoor edges, but their propagation and inclination depend on burial depth. Under shallow conditions, shear bands have larger inclinations, with new bands forming above as initial bands gradually close. Under deep conditions, no new bands form, eventually forming nearly closed shear zones at lower heights. Greater burial depth inhibits shear localization and enhances structural stability.
(5) Depth-based classification: Based on differences in GRC, pressure redistribution, displacement, and failure modes, this study proposes a stress-level classification: 0–479 kPa as shallow and ≥800 kPa as deep. This criterion offers a practical reference for underground space planning, support design, and risk management.

Overall, this work elucidates the burial-depth-dependent mechanisms underlying soil arching and offers a unified framework for interpreting load transfer, deformation, and failure processes in subsurface engineering. Future research should consider stratified soils, dynamic loading, and groundwater to further refine and extend this classification.

Data availability

The data that support the findings of this study are available from the corresponding author upon reasonable request.

CRediT authorship contribution statement

Xing-Tao Lin: Writing – review & editing, Resources, Funding acquisition, Conceptualization. **Deng Wang:** Writing – original draft, Formal analysis, Data curation. **Dong**

Su: Writing – review & editing, Supervision, Conceptualization. **Hui Zeng:** Data curation. **Ruixiao Zhang:** Formal analysis. **Xiangsheng Chen:** Supervision, Project administration.

Declaration of competing interest

The authors declare that they have no known competing financial interests or personal relationships that could have appeared to influence the work reported in this paper.

Acknowledgement

The research was supported by the National Natural Science Foundation of China (Grant Nos. 52208355 and 52378308), and Shenzhen Science and Technology Program (Grant No. JCYJ20250604181459043).

References

Alshibli, K. A., & Hasan, A. (2008). Spatial variation of void ratio and shear band thickness in sand using X-ray computed tomography. *Géotechnique, 58*(4), 249–257.

Bi, Z. Q., Gong, Q. M., Guo, P. J., & Cheng, Q. (2020). Experimental study of the evolution of soil arching effect under cyclic loading based on trapdoor test and particle image velocimetry. *Canadian Geotechnical Journal, 57*(6), 903–920.

Cao, W. P., Xie, Z. D., Yue, Y. X., Zhao, M., Li, Q., & Hu, W. W. (2024). Model tests on 3D soil arching in pile-supported embankments with and without geotextile. *Case Studies in Construction Materials, 20*, e02783.

Chen, R. P., Song, X., Meng, F. Y., Wang, H. L., Liu, Y., & Liu, W. (2025). Experimental investigation on the soil arching effect induced by deep-buried shield tunneling. *Tunnelling and Underground Space Technology, 155*, 106161.

Chevalier, B., Combe, G., & Villard, P. (2012). Experimental and discrete element modeling studies of the trapdoor problem: Influence of the macro-mechanical frictional parameters. *Acta Geotechnica, 7*(1), 15–39.

Consoli, N. C., Winter, D., Leon, H. B., & Filho, H. C. (2018). Durability, strength and stiffness of green stabilized sand. *Journal of Geotechnical and Geoenvironmental Engineering, 144*(9), 04018057.

Costa, Y. D. J., & Zornberg, J. G. (2020). Active and passive arching stresses outside a deep trapdoor. *Acta Geotechnica, 15*(11), 3211–3227.

Costa, Y. D., Zornberg, J. G., Bueno, B. S., & Costa, C. L. (2009). Failure mechanisms in sand over a deep active trapdoor. *Journal of Geotechnical and Geoenvironmental Engineering, 135*(11), 1741–1753.

da Silva Burke, T. S., & Elshafie, M. Z. (2021). Arching in granular soils: Experimental observations of deformation mechanisms. *Géotechnique, 71*(10), 866–878.

Fang, K., Jia, S., Tang, H. M., Zhou, R. Z., Kong, Z., Fu, Y. L., An, P. J., Zhang, B. C., & Wu, Q. (2024). Arching effect in slopes under excavation: Classification and features. *Engineering Geology, 337*, 107563.

Guo, P. J. (2012). Critical length of force chains and shear band thickness in dense granular materials. *Acta Geotechnica, 7*(1), 41–55.

Han, J., & Gabr, M. A. (2002). Numerical analysis of geosynthetic-reinforced and pile-supported earth platforms over soft soil. *Journal of Geotechnical and Geoenvironmental Engineering, 128*(1), 44–53.

Handy, R. L. (1985). The arch in soil arching. *Journal of Geotechnical Engineering, 111*(3), 302–318.

Hu, B. T., Shan, Y., Zhao, Y., Wang, B. L., Zhou, S. H., Alberti, G. S., Ma, W. J., & Demann, B. (2024). Experimental study on tunneling-induced soil arching evolution in pile-raft foundations. *Transportation Geotechnics, 48*, 101340.

Kourkoulis, R., Gelagoti, F., Anastasopoulos, I., & Gazetas, G. (2011). Slope stabilizing piles and pile-groups: Parametric study and design insights. *Journal of Geotechnical and Geoenvironmental Engineering, 137*(7), 663–677.

Lade, P. V. (2003). Analysis and prediction of shear banding under 3D conditions in granular materials. *Soils and Foundations, 43*(4), 161–172.

Lim, A., & Ou, C. Y. (2017). Stress paths in deep excavations under undrained conditions and its influence on deformation analysis. *Tunnelling and Underground Space Technology, 63*, 118–132.

Lin, X. T., Chen, R. P., Wu, H. N., Meng, F. Y., Liu, Q. W., & Su, D. (2022). A composite function model for predicting the ground reaction curve on a trapdoor. *Computers and Geotechnics, 141*, 104496.

Rui, R., Yang, Y., Han, J., Eekelen, S. V., Mu, Z. R., Elabd, M., & Ye, Y. Q. (2024). Progressive development of soil arching and deformations in two- and three-dimensional trapdoor tests. *Géotechnique, 75*(8), 982–994.

Rui, R., Han, J., van Eekelen, S. J. M., & Wan, Y. (2019). Experimental investigation of soil-arching development in unreinforced and geosynthetic-reinforced pile-supported embankments. *Journal of Geotechnical and Geoenvironmental Engineering, 145*(1), 04018103.

Song, X., Miao, C. W., Chen, R. P., Deng, X. N., Zhang, Y., Wang, J. Q., & Chen, X. F. (2025). Experimental and numerical study on the soil arching effect caused by deep-buried shield tunneling. *Underground Space, 24*, 129–141.

Song, X., Wu, H. N., Meng, F. Y., & Chen, R. P. (2023). Soil arching evolution caused by shield tunneling in deep saturated ground. *Transportation Geotechnics, 40*, 100966.

Terzaghi, K. (1943). *Theoretical soil mechanics*. New York: John Wiley & Sons.

Vermeer, P. A. (1990). The orientation of shear bands in biaxial tests. *Géotechnique, 40*(2), 223–236.

Wang, H. L., & Chen, R. P. (2019). Estimating static and dynamic stresses in geosynthetic-reinforced pile-supported track-bed under train moving loads. *Journal of Geotechnical and Geoenvironmental Engineering, 145*(7), 04019029.

Wu, Y. J., Zhao, Y., Gong, Q. M., Zornberg, J. G., Zhou, S. H., & Wang, B. L. (2022). Alternant active and passive trapdoor problem: From experimental investigation to mathematical modeling. *Acta Geotechnica, 17*(7), 2971–2994.

Zhang, H. F., Zhang, P., Zhou, W., Dong, S., & Ma, B. S. (2016). A new model to predict soil pressure acting on deep burial jacked pipes. *Tunnelling and Underground Space Technology, 60*, 183–196.

Zhang, R. X., Su, D., Lin, X. T., Zhu, T. F., Lei, G. P., & Chen, X. S. (2023). Investigation of the soil arching evolution in the ground with or without a tunnel. *Transportation Geotechnics, 43*, 101149.

Zhao, Y., Gong, Q. M., Wu, Y. J., Zornberg, J. G., Tian, Z. Y., & Zhang, X. (2021). Evolution of active arching in granular materials: Insights from load, displacement, strain, and particle flow. *Powder Technology, 384*, 160–175.